Applied Catalysis A, General 713 (2026) 120675

Contents lists available at ScienceDirect

Applied Catalysis A, General

journal homepage: www.elsevier.com/locate/apcata

# $CO_2$- and CO-Conversion to Methanol over promoted CuO/ZnO-based infiltration composite catalyst spheres — Characterization, experimentals and comparative reaction kinetics☆

Carl Fritsch [a,*], Andreas Serwe [a], Sven Jovanovic [b], Hariprasad Ranganathan [c], Marcus Hans [d], Andreas Hutzler [e], Jürgen Dornseiffer [f], Nikolay Kornienko [c]

[a] Forschungsinstitut für Wasserwirtschaft und Klimazukunft an der RWTH Aachen e.V., An der Ölmühle 4, Aachen, 52074, Germany
[b] Institute of Energy Technologies IET-1: Fundamental Electrochemistry, Forschungszentrum Jülich GmbH , Wilhelm-Johnen-Straße, Jülich, 52428, Germany
[c] Institut für Anorganische Chemie, Rheinische Friedrich-Wilhelms-Universität Bonn, Gerhard-Domagk-Straße 1, Bonn, 53121, Germany
[d] Materials Chemistry, RWTH Aachen University, Kopernikusstr. 10, Aachen, 52074, Germany
[e] Helmholtz Institute Erlangen-Nürnberg for Renewable Energy (IET-2), Forschungszentrum Jülich GembH , Cauerstraße 1, Erlangen, 91058, Germany
[f] Institute of Energy Materials and Devices IMD-2: Materials Synthesis and Processing, Forschungszentrum Jülich GmbH, Wilhelm-Johnen-Straße, Jülich, 52428, Germany

ARTICLE INFO

*Keywords:*
Methanol synthesis
RWGS
Infiltration composite
$CO_2$-hydrogenation
Parameter fitting
Reaction kinetics
Carbon monoxide
LHHW

ABSTRACT

Zirconia ($ZrO_2$)-, Ceria ($CeO_2$)-, and Calcium (CaO) -promoted Copper oxide (CuO) Zinc oxide (ZnO) catalysts supported on $\gamma$-alumina spheres are synthesized via incipient wetness impregnation (IWI) and characterized using transmission electron microscopy (TEM), Raman spectroscopy, X-ray Photoelectron Spectroscopy (XPS), and $CO_2$/$H_2$-TPD. Catalytic performance is evaluated for carbon oxide hydrogenation to methanol (MeOH) in mixed carbon oxide synthesis gas, examining both CO and $CO_2$-conversion pathways and MeOH space–time yields (STY). Temperature- and pressure-dependent reaction equilibria for MeOH formation from CO and $CO_2$, as well as the reverse water-gas shift reaction (RWGS) are investigated to demonstrate promoter effects on surface reaction mechanisms and conversion efficiency towards MeOH and $H_2O$. Reaction kinetics are optimized using a previously formulated re-parametrized two-site Langmuir–Hinshelwood–Hougen–Watson (LHHW) model for each catalyst system, providing comparative kinetic parameters for the binary, ternary, quaternary, and quinary catalyst formulations. The kinetic models demonstrate good numerical agreement with experimental data for both the promoted catalysts. Although CO-rich streams produce the highest MeOH production rates in all samples, the promotion through $ZrO_2$ and $CeO_2$ significantly improved both CO and $CO_2$ conversion ($X_C$) compared to the binary CuO/ZnO catalyst formulation.

## 1. Introduction

The direct conversion of $CO_2$ to carbon-based platform chemicals and fuel substitutes promises to become a key technology for the mitigation of industrial carbon emissions and thus plays a vital role in reducing anthropogenic climate impact. In recent years, process development for efficient conversion technologies and advances in materials science for enhanced catalytic activation of the low-reactivity $CO_2$-molecule for hydrogenation to chemical products have become prevalent in respective research fields, with some initial industrial applications being demonstrated commercially lately [1–3]. In this context, it is widely accepted that methanol (MeOH) is a very promising

☆ This document is the result of research projects funded by the German Ministry of Economic Affairs and Energy (49VF190052) and general german funding budget (19I20005D)

* Corresponding author.
*E-mail addresses:* fritsch@fiw.rwth-aachen.de (C. Fritsch), andreas.serwe@alumni.fh-aachen.de (A. Serwe), s.jovanovic@fz-juelich.de (S. Jovanovic), hrangana@uni-bonn.de (H. Ranganathan), hans@mch.rwth-aachen.de (M. Hans), a.hutzler@fz-juelich.de (A. Hutzler), j.dornseiffer@fz-juelich.de (J. Dornseiffer), nkornien@uni-bonn.de (N. Kornienko).
*URLs:* https://www.fiw.rwth-aachen.de/ (C. Fritsch), https://www.fz-juelich.de/de/iet/iet-1 (S. Jovanovic), https://www.chemie.uni-bonn.de/ac/de/startseite (H. Ranganathan), https://www.mch.rwth-aachen.de/cms/~jeuz/mch/ (M. Hans), https://www.hi-ern.de/en (A. Hutzler), https://www.fz-juelich.de/de/imd/imd-2 (J. Dornseiffer), https://www.uni-bonn.de/de/forschung-lehre/forschungsprofil/transdisziplinaere-forschungsbereiche/tra-2-matter (N. Kornienko).

https://doi.org/10.1016/j.apcata.2025.120675
Received 13 July 2025; Received in revised form 1 November 2025; Accepted 3 November 2025
Available online 27 January 2026

potential product derived from $CO_2$ [4]. Well established production processes, a large international infrastructure, and wide applications as both alternative fuel and as a platform chemical as well as comparatively easy adaption of commercial, fossil production processes towards substitutional $CO_2$-introduction as reactant, have led to the beginning commercialization of a regenerative, $CO_2$-based MeOH-production network [3]. While process ramp-up is underway, some essential developmental issues prevail in the industrialization of the commercial $CO_2$-hydrogenation to MeOH on a catalytic level:

- commercial $CuO/ZnO/Al_2O_3$ (CZA)-catalysts show reduced activity towards the hydrogenation of $CO_2$ compared to commercial, fossil derived CO-based reactant streams [5];
- reduced activity can be attributed to the catalytically idle $CO_2$ being harder to activate over CZA than CO, which is far more prevalent in fossil derived SynGas. This necessitates the introduction of different, more aggressive catalyst active sites for the efficient activation and hydrogenation of $CO_2$ or the application of alternative catalyst technologies, improving active catalyst surface area [6,7];
- the stoichiometric co-production of $H_2O$ in the hydrogenation of $CO_2$ can lead to premature deactivation of CZA-catalysts, requiring stabilizing agents for long term stability [3,8];
- the exact mechanisms contributing to both CO- and $CO_2$-hydrogenation are still disputed, making it hard to securely apply catalyst adaptions and optimizations on a molecular level for enhanced conversion of $CO_2$ and optimized long term catalyst stability [8–10];
- while the hydrogenation of $CO_2$, the underlying mechanisms and the selectivity towards MeOH production of developed and optimized catalyst formulas are the focus of many recent studies, the reduction of $CO_2$ to CO and $H_2O$ via reverse water gas shift reaction (RWGS) and its effects on possible commercial application of presented catalysts are often not considered in detail. As single reactor-pass carbon conversion ratios ($X_C$) do not facilitate once-through reactor operation in MeOH-production processes, the unavoidable formation of CO and its reintroduction into the reactor through gas recycling should be considered for catalyst development. Thus, mixed carbon-oxide synthesis gas streams and the interplay between CO and $CO_2$ in the formation of MeOH should be considered, when developing new catalyst formulas and assessing conversion effectiveness [11–13].
- this requires either complex in-situ reaction characterization through methods such as in-situ Diffuse reflectance infrared Fourier transform spectroscopy (DRIFTS) analysis, the application of complex testing facilities, which allow for controlled gas recycling in laboratory environments or the application of kinetics to be able to truly assess application potentials of tested catalyst formulas [14–16].

Many recent studies have thus introduced different metal-oxides as both catalyst promoters in CZA or as carriers and primary active components in bimetallic, ternary, quaternary or quinary catalyst formulas for enhanced hydrogenation of $CO_2$ to MeOH [5]. Herein, especially cerium-oxide ($CeO_2$) and zirconium-oxide ($ZrO_2$) have been identified as very efficient catalysts for the activation of $CO_2$ and its subsequent hydrogenation to MeOH [15,17–20]. The ability of Ceria to form oxygen vacancies on catalyst surfaces allows it to produce active centers for the effective adsorption of $CO_2$ [21]. Furthermore it can exhibit positive influences in lowering the Cu-crystallite sizes through improved dispersion, thus also improving surface-coverage with active centers for both CO- and $H_2$ adsorption [20,22]. Therefore, the use of ceria in MeOH catalysts is able to improve both surface $Cu^+$ formation as well as lowering required activation energies for $CO_2$-activation and subsequent hydrogenation, additionally being able to produce basic active sites for improved adsorption of acidic $CO_2$ [20,23]. Through these effects $CeO_2$ is also able to produce strengthened bonds between metallic Cu and adsorbed CO, inhibiting premature CO desorption and thus preventing $CO_2$-reduction to CO and $H_2O$ through RWGS [24,25].

In a comparable manner, $ZrO_2$ has been shown to positively effect hydrogenation of $CO_2$, increasing catalyst stability due to its slight hydrophobic character and improving dispersion of metal-oxide interfaces that act as active centers in heterogeneous MeOH catalysts [17,19,26]. Additionally $ZrO_2$ can strengthen the binding of reaction intermediates, thus inhibiting CO formation from $CO_2$ and improving selectivity towards MeOH [17,27,28]. Alkaline earth metals have also shown to be able to enhance conversion ratios, when added to CZA, with calcium oxide (CaO) and magnesium oxide (MgO) promoted catalysts showing improved $CO_2$ conversion over CZA-samples, especially at high reaction temperatures [29,30].

Additionally, Multi-metal-oxide interactions in promoted catalysts can enhance the promotional effects of individual additives, improving the conversion efficiencies of multicomponent catalyst formulations compared to single-promoter systems [31,32]. Building on recent developments in direct $CO_2$ hydrogenation to MeOH, we previously introduced four novel carrier catalyst samples designed for efficient $CO_2$-to-MeOH conversion [11]. These samples were prepared as infiltration composites by coating $\gamma$-$Al_2O_3$ spheres with CuO/ZnO (20% CZ) and successively adding $CeO_2$ (20% CZC), $ZrO_2$ (20% CZCZ), and CaO (20% CZCZC), yielding four catalysts with systematically varied metal-oxide promotion.

All catalysts exhibited high selectivity towards CO formation in super-stoichiometric $CO_2$-only feed streams. This observation raises the question of how these materials perform under more realistic industrial conditions, where recycled CO affects the steady-state equilibria of CO- and $CO_2$-hydrogenation as well as RWGS. The present study therefore investigates the promotional effects of $CeO_2$, $ZrO_2$, and CaO in CZA-based catalyst systems under mixed carbon-oxide synthesis conditions. The systematic examination of $CO/CO_2$-ratios herein represents an aspect often overlooked in $CO_2$-to-MeOH studies [10].

A further novelty here lies in the use of $\gamma$-$Al_2O_3$ carrier spheres, which allows a substantial reduction of active-material usage while potentially retaining catalytic performance compared to co-precipitated catalysts [33]. The use of structured $\gamma$-$Al_2O_3$ carriers offers a scalable route for preparing thin, uniform catalyst washcoats with reduced metal loading, helping to minimize diffusional limitations and improve heat transfer — factors often insufficiently controlled in conventional MeOH-synthesis catalyst testing. This design facilitates systematic evaluation of intrinsic kinetic behavior and promoter interactions on the coated catalyst surface.

We combine advanced characterization ($CO_2$/$H_2$-TPD, Raman, TEM, XPS) with kinetic parameter optimization using a tubular fixed-bed reactor model, establishing direct links between promoter-induced structural and electronic modifications and their impact on kinetic parameters. The analysis of step-wise promotional effects on $H_2$ and $O_2$ adsorption enables isolation of single metal-oxide contributions within multi-metal combinations.

Through kinetic parameter optimization for each catalyst, we clarify how $CeO_2$, $ZrO_2$, and CaO influence CO and $CO_2$ conversion to MeOH under industrially relevant conditions. Our results further provide mathematical confirmation that CO-to-MeOH conversion can be excluded from the reaction network under the investigated conditions. Overall, this study expands the kinetic knowledge base for highly promoted CZA catalysts and delivers a methodological foundation for efficient, parallelized kinetic parameter optimization in complex multi-promoter systems.

## 2. Experimental section

### 2.1. Catalyst preparation

Catalyst samples were manufactured by coating high surface area 800μm diameter $\gamma$-$Al_2O_3$ spheres (SASOL, Hamburg Germany) through

**Table 1**
Catalyst composition for the tested samples.

| Sample | CuO | ZnO | $CeO_2$ (mol%) | $ZrO_2$ | CaO |
|---|---|---|---|---|---|
| CZA (Ref) | 68 | 28 | ($Al_2O_3$ - rest) | – | – |
| 20% CZ | 72.2 | 27.8 | – | – | – |
| 20% CZC | 65.0 | 25.0 | 20.0 | – | – |
| 20% CZCZ | 57.8 | 22.2 | 10.0 | 10.0 | – |
| 20% CZCZC | 54.2 | 20.8 | 10.0 | 10.0 | 5.0 |

incipient wetness impregnation method (IWI). In a first step, the maximum adsorption capacity of the carrier for water was determined, yielding an average water-adsorption capacity of 0.64 $g_{H2O}\ g_{Al2O3}{}^{-1}$. Metal nitrate precursors were used for compounding the individual coating for the spheres [11]:

- $Cu(NO_3)_2 \cdot 3\ H_2O$ (Carl Roth GmbH, Karlsruhe Germany)
- $Zn(NO_3)_2 \cdot 4\ H_2O$ (Carl Roth GmbH, Karlsruhe Germany)
- $ZrO(NO_3)_2 \cdot 2.5\ H_2O$ (Alfa Aesar GmbH, Kandel Germany)
- $Ce(NO_3)_3 \cdot 6\ H_2O$ (Alfa Aesar GmbH, Kandel Germany)
- $Ca(NO_3)_2 \cdot 4\ H_2O$ (Alfa Aesar GmbH, Kandel Germany)

To prepare 50 g of the infiltration composite spheres with a catalyst loading of 20 $\%_{wt}$ catalytically active coating, the nitrate salts of the respective metals were first weighed into a beaker according to their molar proportions in the catalyst (Table 1). The compositions were chosen, so that the molar ratio between CuO and ZnO did not change throughout the chosen promotional catalyst compositions according to previously reported optimal ratios in CZA-based catalyst designs [34]. The beaker was filled with water to a total volume of 25.6 ml and the nitrate salts were dissolved under constant stirring. The solutions were mixed with 40 g of the alumina spheres in a porcelain bowl and mixed using a until the liquid was completely absorbed by the carrier spheres. The resulting homogeneous loaded wet composites were dried for 4 h at 100 °C and calcined for 1 h at 350 °C at a heating rate of 2 °C per minute. In each case, 50 g of catalyst spheres with $20\%_{wt}$ CuO/ZnO (20% CZ), $CuO/ZnO/CeO_2$ (20% CZC), $CuO/ZnO/CeO_2/ZrO_2$ (20% CZCZ) and $CuO/ZnO/CeO_2/ZrO_2/CaO$ (20% CZCZC) were obtained. An industrial precipitated CZA reference sample was crushed and sieved to 800–900 µm diameter from 6 mm catalyst pellets. A more detailed catalyst preparation protocol can be found elsewhere [11].

### 2.2. Physical characterization of the samples

Samples surface structure, composition and chemical state were investigated using Raman-Spectroscopy (RS), XPS and High-Angle Annular Dark-Field (HAADF) scanning transmission electron microscopy (HAADF-STEM). Catalyst samples were investigated calcined in their unreduced state after production and drying. Representative Raman-spectra of each unreduced catalyst loaded $Al_2O_3$ carrier sphere were recorded with a WITec alpha 300 R Raman microscope (Ulm, Germany) using a 532 nm excitation laser at a laser power of 7 mW and a 50x magnification Zeiss objective. The microscope utilizes the WITec ultra high throughput spectrometer UHTS 300 VIS–NIR and a 1200 g/mm grating. For each spectrum, 120 accumulations at a integration time of 0.5 seconds were recorded. All spectra were baseline corrected using the spheres algorithm of the WITec Project SIX software (Ulm, Germany).

For TEM-investigation of the samples in their oxidized state, Focused Ion Beam (FIB)-Lamellae were fabricated from the surface of the catalyst spheres at a depth of approx. 8–9 µm. A detailed account of the lamellae manufacturing process is given in the supplementary materials. Lamellae were investigated through HAADF-STEM and energy-dispersive X-ray spectroscopy (STEM-EDXS) on a Talos F200i (Thermo Fisher Scientific) using high tension of 200 kV. Fast Fourier Transformation (FFT) and Inverse fast Fourier Transformation (IFFT) were used for indexing lattice spacing of specific metal-oxide structures of the carrier and its coating based upon the STEM-images. For FFT- and IFFT-analysis, STEM images were processed in the ImageJ environment and automatic FFT- and IFFT-analysis was carried out [35]. Lattice spacing was then derived from FFT plots. A more detailed account of image processing for FFT and IFFT analysis is given in the supplementary materials.

For investigation of Cu- and Zn-species distribution on the unreduced samples as well as identifying catalyst promoter species on the surface, XPS for each catalyst sample was carried out on a Phi5000 VersaProbe II (ULVAC-Phi Inc., USA) using a monochromatic Al K-$\alpha$ source at 1.486 keV. X-ray was set to 50 W and 15 KV for analysis of a 200µm spot on the respective catalyst surfaces. General XPS-surveys were recorded at 187.5 eV pass energy at 0.8 eV and 100 ms per step. Details were recorded for CuO and Cu(OH) in the range of 925 eV to 955 eV and Zn-species in the range of 1010 eV to 1060 eV.

Binding energy for $CO_2$ and $H_2$ was probed through TPD-experiments. $H_2$-TPD was carried out on a Micromeritics 2950 MicroActive (Norcorss, USA). Typically, around 100 µg of sample was used. Samples were dried at 100 °C for at least 3 h in an Ar environment and then loaded into a quartz reactor. Samples were then reduced under a 5% $H_2$ in Ar gas flow from 20 °C–300 °C. We have reported reduction profiles for $H_2$-temperatures programmed reduction analysis (TPR) previously elsewhere [11].

After reduction, the reduced samples were cooled and then flushed with 5% $H_2$ in Ar gas flow from 20 °C to 250 °C at a heating rate of 10 °C/min. Samples were returned to atmospheric pressure and temperature and the gas flow was changed to He. Desorption was then carried out until 700 °C was reached at a heating rate of 10 °C/min and reactor effluent gas was measured using a thermal conductivity detector (TCD). A baseline correction of the recorded values was applied for further handling of the recorded data.

The $H_2$-TPD data was used to determine the copper surface area, copper dispersion, and the degree of reduction for each sample, based upon the previously introduced methodologies by Fichtl et al. (2014), Muhler et al. (1992) and de Carvalho et al. (2002) [36–38]. The total amount of desorbed $H_2$ ($n_{H_2,desorbed}$) was obtained by integrating the TPD-signal between 30–360 °C and applying the calibration factor. This represents the temperature range usually associated with activity of metallic, reduced Cu in Cu-based catalysts. Assuming a 1:1 stoichiometry between H atoms and Cu surface atoms, the number of exposed copper atoms can be expressed as:

$$n_{Cu,surface} = 2 \cdot n_{H_2,desorbed}. \tag{1}$$

The corresponding copper surface area $A_{Cu}$ is calculated from the known surface atom density of polycrystalline copper ($\rho_{Cu} = 1.47 \times 10^{19}$ atoms $m^{-2}$) [36]:

$$A_{Cu} = \frac{n_{Cu,surface} \cdot N_A}{\rho_{Cu}}. \tag{2}$$

Normalization to the catalyst mass ($m_{cat}$) obtains the specific copper surface area in $m^2\ g^{-1}$ catalyst:

$$A_{Cu}^{spec} = \frac{A_{Cu}}{m_{cat}}. \tag{3}$$

The copper dispersion $D$ is further more defined as the ratio of surface copper atoms to the total number of copper atoms in the sample:

$$D = \frac{n_{Cu,surface}}{n_{Cu,total}}, \tag{4}$$

where the total number of copper atoms is obtained from the sample mass, the copper loading ($w_{Cu}$), and the molar mass of copper $M_{Cu}$:

$$n_{Cu,total} = \frac{w_{Cu}}{100} \cdot m_{cat} \cdot \frac{N_A}{M_{Cu}}, \tag{5}$$

Here, $N_A$ is the Avogadro constant, which relates the number of atoms or molecules to the amount of substance in moles, with a value of approximately $6.022 \times 10^{23}$ mol$^{-1}$.

The degree of reduction (DOR) quantifies the fraction of reduced copper relative to the theoretical maximum and is given by:

$$\mathrm{DOR}\ (\%) = \frac{n_{\mathrm{H_2,desorbed}}}{0.5 \cdot n_{\mathrm{Cu,total}}} \times 100. \quad (6)$$

Desorption experiments for $CO_2$ were carried out on a ChemBET Pulsar TPD/TPR instrument (Anton Paar QuantaTec, Boynton Beach, USA). Around 500 mg of each sample were dried in a U-shaped quartz tube at 120 °C overnight in Ar in an outgas station. Then, the samples were installed in the Pulsar instrument and heat-treated at 200 °C (rapid heating in 5 min) for 60 Minutes and subsequently cooled to 50 °C under He flow. $CO_2$-adsorption was started at 50 °C under 5% $CO_2$/He gas flow for 90 Minutes. Then, the gas was switched to He to remove un-adsorbed $CO_2$ for 30 min. Finally, the TPD was performed from 50–600 °C under He with a heating rate of 5 °C/min while the signals were monitored by TCD in the reactor effluent.

### 2.3. Activity testing

Sample activity towards hydrogenation of CO and $CO_2$ as well as reaction equilibria were measured on a custom catalyst test bench with a 70 ml heated stainless steel tubular reactor. The test bench was equipped with gas-dosing mass flow controllers (MFCs) for CO, $CO_2$ and $H_2$ as well as pressure controllers and back pressure valves for control of reactor pressure. The reactor was heated or cooled through a tempered oil thermostat according to a threefold temperature measurement through thermocouples inside the catalyst bed. Reactor effluent composition was measured through a gas chromatography unit (GC, Shimadzu Nexis GC-2030) on a double column configuration with Rt-U-Bond Plot, 30 m × 0.53 mm and mol sieve SH MSieve 5 A – 30 m × 0.53 mm through TCD-measurements of the sample (see Fig. 1). Product gas was cooled and liquid components condensed in a counter current product cooling column with off-gas being depressurized and run through an off-gas analysis chain with inline $CO_2$- and $H_2$-measurements (BlueSense BCP- CO2 and BCP-H2) as well as online measurement of $CO_2$- and CO-content (Emerson NGA2000). A schematic of the test bench is given in Fig. 1. We have reported a more detailed P&ID and description of the reactor setup previously elsewhere [11].

For testing towards conversion activity in mixed carbon-oxide synthesis gas streams, typically 70 ml of catalyst sample were filled into the tubular reactor, with glass wool used as dispersion medium on the top and bottom of the reactor. The samples were reduced with pure $H_2$-flow at 0.5 MPa and 5 l/min $H_2$ flow. For reduction, temperature was increased in 10 °C increments every 10 min until 300 °C was reached. The temperature was then set to the desired reaction temperature and the gas composition and reaction pressure were set using the back pressure controller and the thermostat. Reaction conditions – gas hourly space velocity (GHSV - 8.000 h$^{-1}$–12.000 h$^{-1}$, pressure (2.0–5.0 MPa), temperature (225 °C–275 °C) and gas composition (stoichiometric number SN = 3.0, carbon-oxide-ratio COR: 0.3–1) – were changed at random, with SN and COR calculated as follows:

$$SN = \frac{\dot{n}_{\mathrm{H_2},in} - \dot{n}_{\mathrm{CO_2},in}}{\dot{n}_{\mathrm{CO_2},in} + \dot{n}_{\mathrm{CO},in}} \quad (7)$$

$$COR = \frac{\dot{n}_{\mathrm{CO_2},in}}{\dot{n}_{\mathrm{CO_2},in} + \dot{n}_{\mathrm{CO},in}} \quad (8)$$

Tests results for $COR = 1$ using only $CO_2$ are taken from previously reported results [11]. A comprehensive list of all test conditions tested for all catalyst samples is given in supplementary tables S1- S5. For assessment of sample performance, steady state reaction protocols were applied, where reaction conditions were adjusted and a 15 min timer was set for the reactor system to reach a steady reaction state.

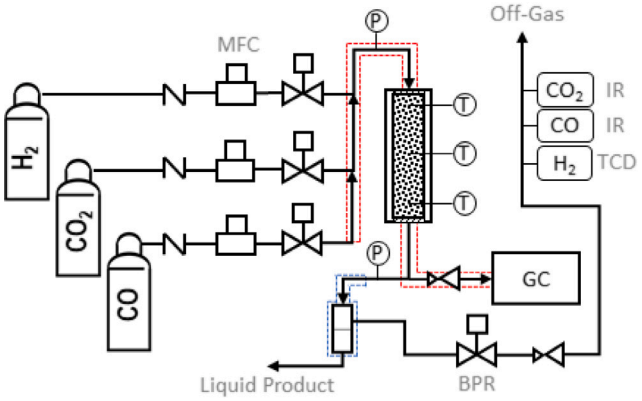


**Fig. 1.** Basic Setup for catalyst activity testing and kinetic performance measurements.

Afterwards, 20 min steady state reaction runs for each parameter combination were carried out. The GC measurements were started at the end of the steady state run, ensuring the measured reactor effluent composition fairly represented a continuous reaction conditions. Selected tests were repeated threefold for each catalyst to ensure recorded results were replicable and represented steady state conditions consistently.

For performance review under the tested conditions, conversion of $CO_2$ ($X_{\mathrm{CO_2}}$), overall carbon conversion ($X_C$), MeOH-production rates ($STY_{\mathrm{MeOH}}$) and MeOH selectivity ($S_{\mathrm{MeOH}}$) were calculated.

$$X_{\mathrm{CO_2}} = \frac{\dot{n}_{\mathrm{CO_2},in} - \dot{n}_{\mathrm{CO_2},out}}{\dot{n}_{\mathrm{CO_2},in}} \quad (9)$$

$$X_C = \frac{\dot{n}_{\mathrm{CO_2},in} + \dot{n}_{\mathrm{CO},in} - \dot{n}_{\mathrm{CO_2},out} - \dot{n}_{\mathrm{CO},out}}{\dot{n}_{\mathrm{CO_2},in} + \dot{n}_{\mathrm{CO},in}} \quad (10)$$

$$S_{\mathrm{MeOH}} = \frac{\dot{n}_{\mathrm{MeOH},out}}{\sum \dot{n}_{products,out}} \quad (11)$$

$$STY_{\mathrm{MeOH}} = \frac{\dot{m}_{\mathrm{MeOH}}}{m_{Catalyst}} \quad (12)$$

$\dot{m}_{\mathrm{MeOH}}$ was derived from the GC measurements under the assumption of conservation of mass and the calculation of overall molar mass of the reactor effluent product. Total mass ($\dot{m}_{tot}$) was calculated from the total mass input, set through the mass flow controllers of the test plant. The product mass flow was then calculated:

$$\dot{m}_i = y_i \frac{\dot{m}_{tot}}{M_{tot}} M_i \quad (13)$$

with

$$M_{tot} = \sum y_i M_i \quad (14)$$

where $y_i$ corresponds to the molar fractions for each gas species and $M_i$ corresponds to the specific molar mass for each species respectively. Reaction equilibria were measured for each catalyst sample at three different temperatures (225 °C, 250 °C and 275 °C) and three reaction pressures (2.0 MPa, 3.5 MPa and 5.0 MPa) retaining a set SN of 3.0 for guaranteed surface coverage with hydrogen and a set industrial GHSV of 10.000 h$^{-1}$. Measurements were started at COR = 1 and reactor effluent COR was measured using the IR-detectors at the reactor exit. COR was taken from the IR-measurements and set as input gas composition while retaining the COR and GHSV mentioned above. After each adaption of influent gas composition, normalization of effluent measurements or at least 10 min are timed as an indicator of steady-state reaction conditions on the catalyst surface. Once steady state has been reached, a new influent gas composition is set. This is repeated until the change in effluent COR was too small for the thermal gas dosing units to be able to reproduce the COR change. After the final iteration of the influent gas changes, GC measurements were started for the steady-state CO- and $CO_2$-conversion equilibria.

### 2.4. Reaction kinetics

The rigorous mechanisms and kinetics of MeOH formation in CZA-catalysts are still widely disputed [12,31,39,40]. Additionally, promotion of CZA leads to a change in surface activity, the creation of new, different or adapted active sites for reactant and product adsorption and thus to the change of kinetic parameters in mathematical representation of the reaction mechanisms. This facilitates the generation of new kinetic models for new catalyst formulas or the adaption of existing mechanistic models to fit test data for new catalyst compositions. Several competing kinetic models for the calculation of MeOH reactions exist, that have been widely adapted for the use of changed catalyst formulas and are able to reproduce test results for novel MeOH catalysts well [31,41–43]. Meanwhile, most available kinetic models are based upon the Langmuir–Hinshelwood–Hougon–Watson model, which takes into account the availability of active centers in the catalyst and provides a numerical approach to the description of different species competing for the same active centers in the catalyst [44]. Herein, most existing models use single-site (SS), double-site (DS) or three-site (TS) adsorption terms (AT) for the mathematical representation of the underlying reaction mechanisms.

Here $H_2$, $CO_2$ and CO all compete for the same active sites in SS-AT, $H_2$ and CO/$CO_2$ are assigned to different sites in DS-AT and $H_2$, $CO_2$ and CO all adsorb on different neighboring acting points in TS-AT. More in-depth reviews of existing models for the calculation of MeOH-synthesis processes, the synthesis of new models for novel catalyst test data and their applications have been reported elsewhere in great detail [31,42,44–46]. From existing models, the DS-AT model proposed by Graaf et al. (1988) [47] has shown to reproduce CZA-test and also novel MeOH catalyst test data very well. This, it has been applied in diverse research work concerning both the modeling of MeOH-synthesis processes and the refit of the model parameters to different kinetic data from CZA but also to adapted catalyst formulas [16]. Several studies have found that parameter refitting for the Graaf-model yields mathematically superior results compared to refits carried out for other models, even in application with $CeO_2$ and $ZrO_2$ promoted CZA based catalysts [31,41]. Compared to many other models, the Graaf-model utilizes kinetic equations ((15)–(17)/(28)–(30)) for both $CO_2$- and CO-hydrogenation to MeOH, making it a fitting candidate for tests conducted in mixed carbon oxide streams and model application towards the conversion of CO and $CO_2$ to MeOH and its byproducts.

$$CO_2 + 3H_2 \rightleftharpoons CH_3OH + H_2O \quad \Delta_r H^O = -49.4 \frac{kJ}{mol} \tag{15}$$

$$CO + 2H_2 \rightleftharpoons CH_3OH \quad \Delta_r H^O = -90.5 \frac{kJ}{mol} \tag{16}$$

$$CO_2 + H_2 \rightleftharpoons CO + H_2O \quad \Delta_r H^O = 41.1 \frac{kJ}{mol} \tag{17}$$

Based upon the cited studies, the Graaf-model is herein applied for adapting and refitting optimized reaction kinetics for all four presented catalyst samples. For a deepened understanding of the mechanisms contributing to $CO_2$ conversion to CO and MeOH and the interplay between CO and $CO_2$ in the formation of both MeOH and $H_2O$ in the multi-metal-oxide catalyst formulas, a distinct kinetic parameter-set was fitted to the existing model for each sample using a custom python script, optimizing the kinetic model parameters inside a pseudohomogeneous plug-flow-reactor (PFR) model to the test result data.

#### 2.4.1. Mass transfer limitations

In heterogeneous catalysis at high temperatures and high reaction rates, mass transfer limitations can occur that influence the outcome of kinetic tests. Formulation of kinetic models based upon these tests can lead to inaccurate results if not corrected for possible mass transfer limitations [16].

Thus, external and internal limitations of mass transfer and diffusion have to be taken into account in optimizing reaction kinetics [42]. The Weisz-parameter is a good measure to approximate the effect of diffusion limitation in catalyzed reaction setups [48]. It is defined as follows:

$$\Phi_{WP} = \frac{r_{obs} \cdot R_p^2}{D_{eff} \cdot C_{surface}} \tag{18}$$

with $r_{obs}$ being the observed or measured reaction rate of a single species involved in the reaction. The effective Diffusivity of a single species under certain reaction conditions $D_{eff}$ is defined as

$$D_{eff} = \frac{\varepsilon}{\tau} \cdot \frac{D_{AB} \cdot D_K}{D_{AB} + D_K} \tag{19}$$

with the binary diffusivity $D_{AB}$ being defined as

$$D_{AB} = \frac{1.00 \times 10^{-3} \cdot T^{1.75} \cdot \sqrt{\frac{1}{M_A} + \frac{1}{M_B}}}{P \cdot [(\Sigma v_A)^{1/3} + (\Sigma v_B)^{1/3}]^2} \tag{20}$$

and the Knudsen diffusivity $D_{KN}$ being defined as

$$D_K = \frac{2}{3} \cdot r_{pore} \cdot \sqrt{\frac{8RT}{\pi M}} \tag{21}$$

In this instance, $r_{pore}$ represents the measured average pore volume of the applied catalyst, $\tau$ represents the tortuosity of a catalyst, $\epsilon$ refers to the void fraction of a catalyst type, and $C_{surface}$ refers to the effective concentration of the investigated reaction species in the reactor. For calculation of $\Phi_{WP}$ textural properties of the catalyst and additional properties of the alumina-carriers like $\tau$ where taken from previous studies [11,49]. In many instances, internal mass transfer limitations are neglected in kinetic modeling, if $\Phi_{WP}$ assumes values below 0.1 for most test conditions [46].

For testing the reaction setup towards external mass transfer limitation, the Mears criterion is often applied. The dimensionless Mears criterion number is herein defined as:

$$\text{Mears} = \frac{r_{obs} \cdot d_p \cdot \rho_b}{k_c \cdot C_{surface}} \tag{22}$$

Here the species concentration on the catalyst surface is calculated from the ideal gas law:

$$C_{surface} = \frac{P_i}{RT} \tag{23}$$

The mass transfer coefficient $k_c$ is furthermore defined as:

$$k_c = \frac{Sh \cdot D_{AB}}{d_p} \tag{24}$$

The Sherwood number Sh is calculated from

$$Sh = 2 + 0.6 \cdot Re^{0.5} \cdot Sc^{0.33} \tag{25}$$

with the Reynolds number Re and the Schmidt Sc number being defined as

$$Re = \frac{\rho_g \cdot u_s \cdot d_p}{\mu_g} \tag{26}$$

$$Sc = \frac{\mu_g}{\rho_g \cdot D_{AB}} \tag{27}$$

In kinetic modeling, external mass transfer limitations and their influence on the kinetic reactor model are often times neglected if the Mears criterion does not assume values above 0.15 for most of the reaction conditions. In these cases, the reaction is kinetically controlled and intrinsic reaction rates are slow enough for diffusion and mass transfer between solid and gas phases in the reactor not to limit the rates [42,46]. In this work we tested the reaction conditions for both the Weisz- and the Mears-criterion, looking at internal and external mass transfer and diffusion limitations. $CO_2$, $H_2$, MeOH and $H_2O$ were tested for limitations for all catalyst samples in all applied reaction conditions.

*2.4.2. Kinetic model deduction*

The Graaf-model is based around a two-site adsorption mechanism, where CO and $CO_2$ compete for one type of active site in the catalyst compound and $H_2$ and $H_2O$ adsorb on a second. In the kinetic model, rate equations are used for CO- and $CO_2$-hydrogenation towards MeOH generation and a third for RWGS. The rate equations use adsorption and kinetic constants, to which the kinetic parameters of the model are fitted based on the tests conducted in the laboratory reactor setup. Graaf et al. (1988) based their set of reactions on three macroscopic reactions occurring simultaneously, each made up of several different elementary reaction steps, from which they derived their kinetic expressions. The reaction complex for each of the three reactions included in the mechanisms is given in Table 2 [46,47].

The original model suggests four possible steps for CO-hydrogenation, two steps in $CO_2$-reduction to CO and $H_2O$ through RWGS and six possible steps for the hydrogenation of $CO_2$ to MeOH and $H_2O$ [47]. The latter corresponds to the formate pathway of $CO_2$-hydrogenation to MeOH, which is accepted to account for most of the $CO_2$ being converted in CZA catalysts, especially in high COR environments [44,50]. Recent studies show, that initial hydrogenation steps for both CO and $CO_2$ in MeOH synthesis as well as adsorption and desorption processes on the catalyst surface do not influence reaction kinetics much [51]. Therefore, adsorption, initial hydrogenation of adsorbed carbon oxide species and desorption of products are emitted as possible reaction steps accounted for in the later optimization of parameters, thus also reducing calculation time and streamlining the multi-stage fitting procedure. Overall, this study therefore concentrates on fitting an optimal model based upon the reaction steps A2–A4, B1–B2 and C2–C5. For $CO_2$-hydrogenation, this represents most of the formate-reaction pathway, although multiple steps of the formulated mathematical model can account for other reaction steps in carbon-oxide-hydrogenation to MeOH following alternative intermediate pathways. One limitation of the model proposed by Graaf et al. therefore lies in the composition of the driving force terms, as they can mathematically represent different reaction intermediates, also containing some found in reaction pathways other than the formate route [52].

Overall, model deduction from the proposed reaction steps yields a possible 24 different rate equation combinations, that are differentiable by their driving force (DF) groups, with equilibrium constants taken from the recent update for CZA catalysts by Graaf et al. (2016) [53]. This constitutes a second limitation of the proposed model, as reaction equilibrium constants are assumed to be equal to those of pure precipitated CZA-catalysts. The entire model can be constructed in principle as follows:

$$r_{CO} = k_{CO} \cdot K_{CO} \cdot \frac{DF_{CO,A_i}}{Denominator} \tag{28}$$

$$r_{RWGS} = k_{CO_2} \cdot K_{CO_2} \cdot \frac{DF_{RWGS,B_i}}{Denominator} \tag{29}$$

$$r_{RWGS} = k_{CO_2} \cdot K_{CO_2} \cdot \frac{DF_{CO_2,C_i}}{Denominator} \tag{30}$$

with the denominator compounded from two terms — one each for each represented active site in kinetic modeling:

$$Denominator = (1 + K_{CO}\, p_{CO} + K_{CO_2}\, p_{CO_2})(p_{H_2}^{0,5} + \frac{K_{H_2O}}{K_{H_2}^{0,5}}\, p_{H_2O}) \tag{31}$$

Inside the kinetic model, the adsorption constants are described though the Van't Hoff approach:

$$K_{ads,i} = e^{\frac{\Delta S_{i,ads}}{R}}\, e^{\frac{\Delta H_{i,ads}}{RT}} \tag{32}$$

The exponential relation between standard adsorption entropy and reaction temperature is herein fixed to a single parameter, leading to the following expression for the kinetic adsorption terms for the kinetic model in this work containing a single pre exponential factor and the calculated, adsorption enthalpy:

$$K_{ads,i} = a_i\, e^{\frac{\Delta H_{i,ads}}{RT}} \tag{33}$$

Kinetic constants are expressed through the Arrhenius approach, leading to following representation as kinetic isotherms containing the activation energy of each reaction step and a pre-exponential factor as fitting parameters:

$$k_i = b_i\, e^{\frac{Ea_i}{RT}} \tag{34}$$

The kinetic model can then be written as a compound of three rate equations, with its dependency on species concentration in the reactor represented by species partial pressures. Exponential weighting of the $H_2$ partial pressure additionally depends on the chosen reaction step, which correlates directly to the pending H $*$-species involved in the outstanding reaction steps towards product formation. In their original work from 1988, Graaf et al. found the following rate equations to represent the reaction complex in the CZA-catalyst most accurately, corresponding to $H_2CO$ $*$-hydrogenation as RDS in MeOH formation from CO, HCOO $*$-hydrogenation as RDS in RWGS and $H_2COO$ $*$-hydrogenation in MeOH formation from $CO_2$. AS low pressures and low temperatures are applied in this work, partial pressures are applied instead of fugacities, as applied in the original model formulation, thus avoiding calculation of computationally complex thermodynamic models in model discrimination and parameters optimization [47].

$$r_{MeOH,CO} = k_1\, K_{CO} \left( p_{CO}\, p_{H_2}^{1,5} - \frac{p_{MeOH}}{p_{H_2}^{0,5}\, K_{eq,1}} \right) D^{-1} \tag{35}$$

$$r_{RWGS} = k_2\, K_{CO_2} \left( p_{CO_2}\, p_{H_2} - \frac{p_{H_2O}\, p_{CO}}{p_{H_2}\, K_{eq,2}} \right) D^{-1} \tag{36}$$

$$r_{MeOH,CO_2} = k_3\, K_{CO_2} \left( p_{CO_2}\, p_{H_2}^{1,5} - \frac{p_{H_2O}\, p_{MeOH}}{p_{H_2}^{1,5}\, K_{eq,3}} \right) D^{-1} \tag{37}$$

The denominator for each of the rate equations is identical, as both active center interactions described by the denominator, are involved in all three reactions. It can be expressed as follows, where the adsorption constants for $H_2$ and $H_2O$ are compounded into one value fitted through a single Arrhenius isotherm.

$$D = (1 + K_{CO}\, p_{CO} + K_{CO_2}\, p_{CO_2})(p_{H_2}^{0,5} + \frac{K_{H_2O}}{K_{H_2}^{0,5}}\, p_{H_2O}) \tag{38}$$

The exact composition of the driving force group is deducted from the scheme of elementary reaction steps given in Table 2.

*2.4.3. Reactor modeling*

The 1D PFR-model is implemented as follows:

Mass balance

$$-u_s \frac{dc_i}{dz} + \rho_{cb} \sum_{n=1}^{n_r} r_{ij} = 0 \tag{39}$$

Energy balance

$$-u_s c_p \frac{d\rho_g T}{dz} = \rho_g \sum_{n=1}^{n_r} (-\Delta H_i)_j r_j + \frac{4U}{D_t}(T_w - T) \tag{40}$$

Here, $u_s$ represents the superficial gas velocity, $c_i$ represents the concentration of species i along the 1D $z$-axis of the reactor, $\rho_c$ represents the bulk catalyst density and $r_{ij}$ represents the reaction rates of the three competing reaction which the parameters are fitted to during the optimization. Furthermore, $u_s$ is updated along the $z$-axis of the reactor according to the gas density change through consumption of reactants and production of MeOH, $H_2O$ and CO. $\rho_g$, $D_t$, $T$ and $T_w$ represent the apparent density of the gas along the $z$-axis of the reactor model, the diameter of the reactor tube and local reactor temperature and reactor

**Table 2**
Mechanism on the catalyst surface with kinetic model driving forces.

| Step | Reaction | Driving force |
|---|---|---|
| Adsorption | | |
| 1 | $CO + s1 \rightleftharpoons CO^{(s1)}$ | – |
| 2 | $CO_2 + s1 \rightleftharpoons CO_2^{(s1)}$ | – |
| 3 | $H_2 + 2s2 \rightleftharpoons 2H^{(s2)}$ | – |
| 4 | $H_2O + s2 \rightleftharpoons H_2O^{(s2)}$ | – |
| CO hydrogenation pathway | | |
| A1 | $CO^{(s1)} + H^{(s2)} \rightleftharpoons HCO^{(s1)} + s2$ | $p_{CO} \cdot p_{H_2} - \frac{p_{CH_3OH}}{p_{H_2}^2 \cdot K_{eq,3}}$ |
| A2 | $HCO^{(s1)} + H^{(s2)} \rightleftharpoons H_2CO^{(s1)} + s2$ | $p_{CO} \cdot p_{H_2}^2 - \frac{p_{CH_3OH}}{p_{H_2} \cdot K_{eq,3}}$ |
| A3 | $H_2CO^{(s1)} + H^{(s2)} \rightleftharpoons H_3CO^{(s1)} + s2$ | $p_{CO} \cdot p_{H_2}^3 - \frac{p_{CH_3OH}}{K_{eq,3}}$ |
| A4 | $H_3CO^{(s1)} + H^{(s2)} \rightleftharpoons H_3COH + s1 + s2$ | $p_{CO} \cdot p_{H_2}^4 - \frac{p_{CH_3OH} \cdot p_{H_2}}{K_{eq,3}}$ |
| Reverse water-gas shift (rWGS) pathway | | |
| B1 | $CO_2^{(s1)} + H^{(s2)} \rightleftharpoons HCOO^{(s1)} + s2$ | $p_{CO_2} \cdot p_{H_2} - \frac{p_{H_2O} \cdot p_{CO}}{p_{H_2} \cdot K_{eq,2}}$ |
| B2 | $HCOO^{(s1)} + H^{(s2)} \rightleftharpoons CO^{(s1)} + H_2O^{(s2)}$ | $p_{CO_2} \cdot p_{H_2}^2 - \frac{p_{H_2O} \cdot p_{CO}}{K_{eq,2}}$ |
| $CO_2$ hydrogenation pathway | | |
| C1 | $CO_2^{(s1)} + H^{(s2)} \rightleftharpoons HCOO^{(s1)} + s2$ | $p_{CO_2} \cdot p_{H_2} - \frac{p_{CH_3OH} \cdot p_{H_2O}}{p_{H_2}^3 \cdot K_{eq,1}}$ |
| C2 | $HCOO^{(s1)} + H^{(s2)} \rightleftharpoons H_2COO^{(s1)} + s2$ | $p_{CO_2} \cdot p_{H_2}^2 - \frac{p_{CH_3OH} \cdot p_{H_2O}}{p_{H_2}^2 \cdot K_{eq,1}}$ |
| C3 | $H_2COO^{(s1)} + H^{(s2)} \rightleftharpoons H_3COO^{(s1)} + s2$ | $p_{CO_2} \cdot p_{H_2}^3 - \frac{p_{CH_3OH} \cdot p_{H_2O}}{p_{H_2} \cdot K_{eq,1}}$ |
| C4 | $H_3COO^{(s1)} + H^{(s2)} \rightleftharpoons H_3CO^{(s1)} + H_2O^{(s2)}$ | $p_{CO_2} \cdot p_{H_2}^4 - \frac{p_{CH_3OH} \cdot p_{H_2O}}{K_{eq,1}}$ |
| C5 | $H_3CO^{(s1)} + H^{(s2)} \rightleftharpoons H_4CO^{(s1)} + s2$ | $p_{CO_2} \cdot p_{H_2}^5 - \frac{p_{CH_3OH} \cdot p_{H_2O} \cdot p_{H_2}}{K_{eq,1}}$ |
| C6 | $H_4CO^{(s1)} + H^{(s2)} \rightleftharpoons H_3COH + s1 + s2$ | $p_{CO_2} \cdot p_{H_2}^6 - \frac{p_{CH_3OH} \cdot p_{H_2O} \cdot p_{H_2}^2}{K_{eq,1}}$ |

wall temperature for the heat loss term. As the temperature is kept at quasi isothermal conditions, the loss term can be omitted for the energy balance. Reaction enthalpies $-\Delta H_{ij}$ are considered to be constant and are taken from [45]. For calculating the reaction rates based upon the reactor model and optimizing the kinetic parameters towards a good numerical fit to the test data, the differential equations for the $z$-axis resolved energy and mass balances inside the reactor are solved using pythons `solve_ivp` function and its BDF-solver.

### 2.4.4. Parameter optimization

A custom python script, which is described in more detail in the supplementary materials, is used to fit the kinetic parameters of the Graaf-model to the herein recorded test data based upon the reactor model applied to represent the tubular reactor used in this study. A base objective function for minimizing the root mean squared error (RMSE) of calculated reactor effluent partial pressures of the product species MeOH and $H_2O$ is used for optimizing the 13 fitting variables from the original Graaf-model.

$$F_{obj} = \sum [q_{MeOH} \left(\frac{p_{MeOH,\ calc} - p_{MeOH,\ exp}}{p_{MeOH,\ exp}}\right)^2 - q_{H_2O} \left(\frac{p_{H_2O,\ calc} - p_{H_2O,\ exp}}{p_{H_2O,\ exp}}\right)^2] \quad (41)$$

Here $q_{MeOH}$ and $q_{H_2O}$ are weighting factors for weighting MeOH- and $H_2O$-reactor exit partial pressures inside the objective function. Alternative approaches for construction of the objective function, where the model was optimized towards different combinations of effluent species partial pressures or holistic approaches utilizing the entire composition of the reactor effluent in the minimization function were also tested. After evaluation of base-line model performance for different variations of the objective function through WPI (refer to supplementary materials - statistical analysis), the approach minimizing only residuals for the two product $H_2O$ and MeOH was chosen, due to its superior performance in estimating product partial pressures. As most models yielded the least optimal results in calculating $H_2O$-partial pressures in the reactor effluent, weighting factors were introduced for better control of the optimization results towards optimizing $R^2$ for $H_2O$ estimation. $q_{MeOH}$ was usually set to 1 while $q_{H_2O}$ was commonly set to 3, as $H_2O$-production rates from RWGS and $CO_2$-hydrogenation played an essential role in the quality of the model fit and yielded the highest amount of uncertainty in model deduction. While adapting the Graaf-model towards the herein presented test data, it was discovered, that the original model did not accommodate well for the calculation of tubular reactors in all reaction conditions, with conversion rates often assuming unlikely values at reactor entry and reaching reaction and concentration equilibria very quickly or oscillating strongly due to the very abrupt changes in local concentration differentials along the $z$-axis of the reactor. As very abrupt reactor concentration differentials are unlikely in a real-world application, the herein tested objective function was expanded to include penalties (P) for oscillating concentration profiles and very abrupt changes in reactant concentration along the z-profile [16]:

$$P = \begin{cases} \sum_{i \in \{MeOH, H_2O\}} 0.1 \times F_{osc,\ i} & \text{if } F_{osc,\ i} > 1 \\ 0 & \text{otherwise} \end{cases} \quad (42)$$

with the oscillation-function being defined as

$$F_{osc,\ i} = \sum_{z=0}^{Z} H(|\text{sgn}(\frac{dC_i}{dz}(z+1)) - \text{sgn}(\frac{dC_i}{dz}(z))|) \quad (43)$$

and with the Heaviside-step function (H) for detection of oscillations inside the concentration profiles defined as

$$H(x) = \begin{cases} 1 & \text{if } x > 0 \\ 0 & \text{if } x \leq 0 \end{cases} \quad (44)$$

For optimization of the reaction parameters, a multi-strategy, parallel programming optimization script was implemented. As all three reactions – $CO_2$-hydrogenation, CO-hydrogenation and RWGS – are based upon a selection of possible rate-determining steps (RDS) inside the proposed reaction mechanisms for the three considered reactions, a total of 24 combinations of these rate determining steps is possible for the overall reaction set. Thus, a parallel approach to optimization is applied, where all possible combinations of RDS for the three reactions involved in the complex can be solved simultaneously. The full overview over the reaction steps considered in this work is given in Table 2. The script used for optimization is published in a repository alongside this work [54].

End results of optimization problems can rely heavily on the initial guess [31,42]. To ensure optimization results were independent of the initial guess required by pythons fmin-function, multiple initial

optimization runs with limited optimization iterations were carried out for every possible rate model. Each initial strategy was defined by the use of a different set of initial guess parameters. The initial guesses used were the original parameters reported by Graaf et al. (1988) and Poto et al. (2022) [31,47]. Additionally, a third strategy was run with the initial guess randomized inside feasible parameter bounds. After completion of the preliminary strategies, the resulting parameters were compared and the initial guess yielding the best short-term optimization results was chosen for full optimization of the parameters.

Minimization of the objective function and applied penalties was carried out in a two-stage process, where the objective- and penalty function was minimized using the downhill-simplex-algorithm from pythons fmin-library. After initial optimization of a parameter set, the optimized kinetic parameter where handed over to a second optimization run using a limited memory Broyden–Fletcher–Goldfarb–Shannon (L-BFSG-S) algorithm for parameter refinement. Both the downhill-simplex-algorithm, as well as the L-BSFG-S algorithm are constrained optimization procedures. Optimizer constraints were applied for both the rough as well as the detailed optimization run with an optimization timeout set to 15.000 iterations inside each optimized rank. The constraints were chosen liberally, with upper limits for $\Delta H_{i,ads}$ and lower limits for $\Delta H_{i,ads}$ that inhibit the calculation of physically unfeasible models. A table containing the list of constraints is given in supplementary table S6. The confidence intervals of the estimated kinetic parameters were determined a posteriori from the finite-difference approximation of the Hessian matrix of the objective function. A full description of the calculation for 95% confidence intervals is given in the supplementary materials. Further statistical analysis of the optimization results is also described in detail in the Supplementary Materials.

#### 2.4.5. Model sensitivity

To quantify the individual and interactive effects of kinetic parameters on reactor performance across different $CO_2$/CO ratios (COR), we employed Sobol-global sensitivity analysis using Python's SALib sensitivity analysis package. The Sobol approach herein decomposes the total variance of model outputs into contributions from individual model parameters and their respective interactions with each other using a variance based (ANOVA) approach and applying Monte Carlo principles for generation of a numerical model space for analysis of the parameter contributions [55]. In our sensitivity analysis, the first-order sensitivity index, $S_i$, represents the main effect of variable model parameter $X_i$ on a chosen model output value. It represents the probabilistic fraction of model output that can be attributed directly to the variation of the input parameter in question [56]:

$$S_i = \frac{V_{X_i}[E_{X_{\sim i}}(Y|X_i)]}{V(Y)} \tag{45}$$

where $V_{X_i}$ denotes the variance of an output value over parameter $X_i$, $E_{X_{\sim i}}$ is the expected value over all parameters except $X_i$ derived from the construction of the Monte Carlo sample space of the kinetic model, and $V(Y)$ is the total variance of the model output value $Y$.

The total order sensitivity index, $S_{T_i}$, captures both main- or first-order effects and all interactive effects of higher order that involve the parameter $X_i$. Thus, it represents a summary of the direct effect parameter variation $X_i$ has on model output variance and of interactive effects including $X_i$ have on the model variance:

$$S_{T_i} = \frac{E_{X_{\sim i}}[V_{X_i}(Y|X_{\sim i})]}{V(Y)} = 1 - \frac{V_{X_{\sim i}}[E_{X_i}(Y|X_{\sim i})]}{V(Y)} \tag{46}$$

The interaction effect is quantified as $S_{int_i} = S_{T_i} - S_i$, representing the additional variance contribution from the interaction of the parameters. To assess parameter importance across multiple model outputs and operating conditions as well as all fitting parameters, we computed summary statistics for each of the parameters first:

- the average main effect, $\overline{S_i} = \frac{1}{n_{outputs}} \sum_{j=1}^{n_{outputs}} S_{i,j}$
- the maximum main effect across all outputs, $S_{i,max} = \max_j(S_{i,j})$
- the minimum main effect, $S_{i,min} = \min_j(S_{i,j})$

Values of $S_i > 0.01$ indicate parameters with significant individual influence, while large differences between $S_{T_i}$ and $S_i$ suggest strong parameter coupling effects [56]. Parameters exhibiting high $S_{i,max}$ values are critical for at least one model output, whereas those with consistently high $\overline{S_i}$ values are important across all reactor performance metrics.

This analysis enables identification of critical kinetic parameters whose accurate determination are essential for reliable reactor predictions, particularly when SynGas-composition varies across different COR operating conditions in MeOH synthesis. These indices allow for the identification of the most influential kinetic parameters affecting MeOH and $H_2O$ formation, and side reactions in the reactor [57].

For further evaluation of model sensitivity towards the applied kinetic fitting parameters in the Graaf-base model, parameters are ranked by their average impact on model results and the identified cross-sensitivities. Larger values herein represent large individual and compounded effects of selected model parameters towards selected kinetic model output variables. For detailed evaluation of the overall model sensitivity towards selected kinetic parameters, MeOH production, $CO_2$ conversion, $H_2O$ production and overall MeOH selectivity were chosen as model output variables.

## 3. Results

### 3.1. Material characterization

#### Physical surface characterization by Raman, XPS and HAADF-STEM

Results from TEM-analysis are given in Fig. 2, results from Raman- and XPS-analysis are given in Fig. 3. Cross sections of 2 μm deep FIB-lamellae if the produced catalyst spheres can be seen in the top row of figures with magnified images and metal concentration profiles added in the mid row of figures. As is expected the highly promoted catalyst samples show a less uniform distribution of metal mesh alignment. All strongly magnified images (5 nm) show clear agglomerates of metal oxides over the $Al_2O_3$-carrier in separated groups, which is clearly marked by the alteration of metal grid orientation in these agglomerates. This is most clearly shown in 20% CZCZC, where the highest level of catalyst promotion leads to the formation of widely dispersed metal oxide accumulations. The accumulations do not span more than a few nm in diameter. This leads to the formation of plentiful multiple metal oxide interfaces, which have been shown to act as active centers for the adsorption of $CO_2$ and CO in MeOH synthesis and thus enhance activation of both carbon oxides for further hydrogenation, especially in $CeO_2$/$ZrO_2$-promotion and in CZA-catalysts [58,59].

Based upon the HAADF STEM-images, integrated STEM-EDXS line profiles were plotted for analysis of the penetration of the catalytically active metal oxide species into the alumina-carrier. The profiles are given in Fig. 2 (d1)–(d4). Additionally, images of Cu and Zn penetration are given in Fig. 2 (b1)–(b4). As alumina is used as carrier, all profiles show a quite even profiles for alumina. Concerning Cu and Zn, which were used as a binary active catalyst complex in all four samples, a slight decline in signal intensity can be observed in the first 200–300 nm of the catalyst surface, with 20% CZCZ and 20% CZCZC showing the strongest agglomeration of Cu on the outer carrier surface with signal intensity and thus the elemental concentration of Cu decreasing the strongest in comparison to 20% CZ and 20% CZC. In 20% CZC a Ce deposit is clearly visible in both the 200 nm magnification spectrum-image and the concentration profile, with Ce-concentration high at the outer surface of the carrier sphere and decreasing to near zero towards the bottom of the line profile. At the same time, Cu and Zn concentration do not change much over the evaluated line, indicating good infiltration of the active catalyst components into the porous

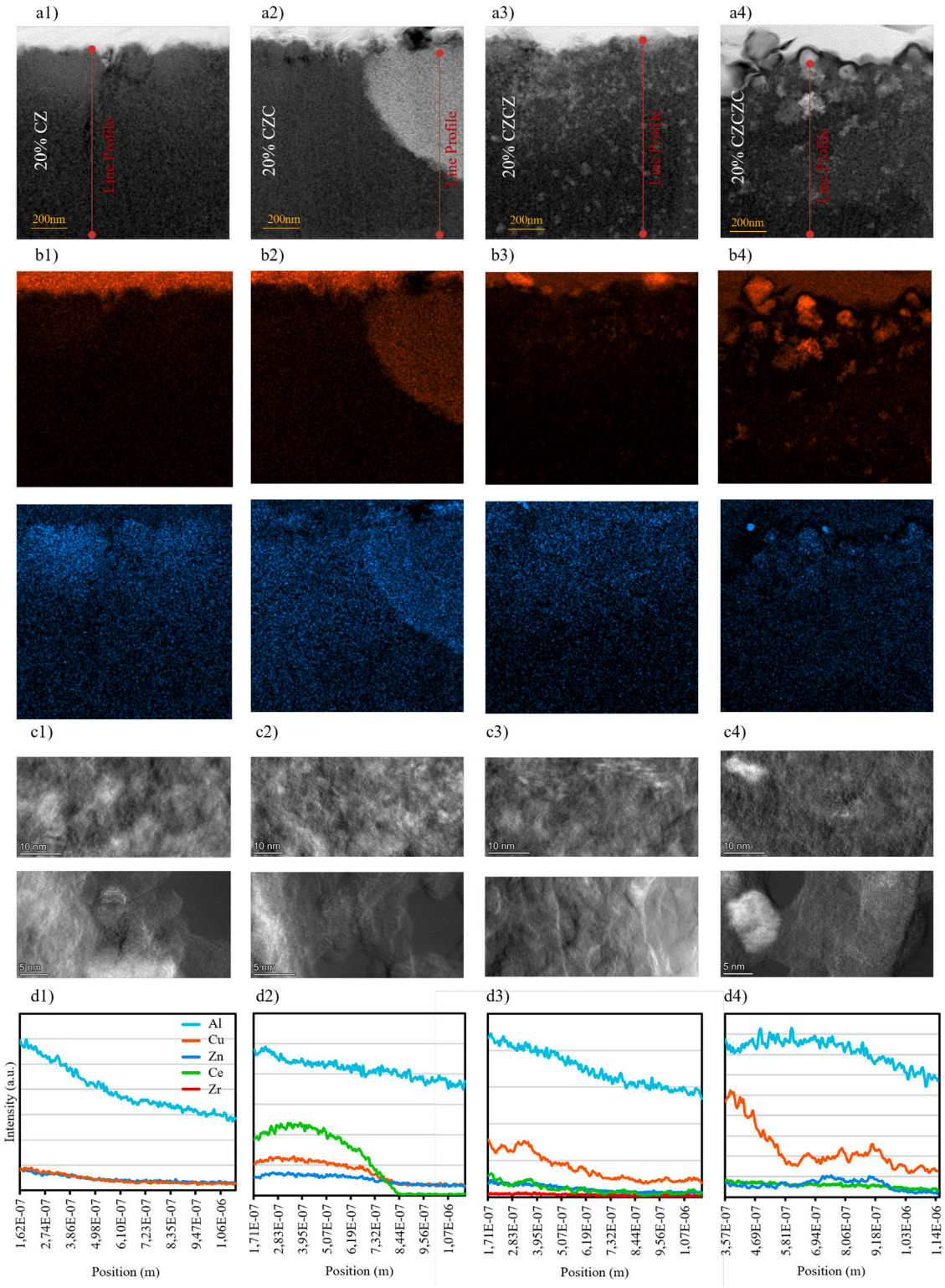


**Fig. 2.** Detail HAADF-STEM-images of the FIB-Lamellae cross sections for all four herein presented infiltration composite catalysts. (a1–a4) HAADF-STEM-images of the catalyst cross sections at 200 nm (b1–b4) STEM-EDX-spectrum mappings for Cu ad Zn (c1–c4) 10 nm and 5 nm magnification of the lamellae cross sections (d1–d4) Integrated STEM-EDXS line profiles for the detected elements over the 2 μm FIB lamellae radial cross sections.

carrier. This implies somewhat inconsistent infiltration in some parts of the 20% CZC catalyst. In 20% CZCZC Zr could not be detected along the plotted line profile. Additional HAADF STEM-characterization and enhanced EDX-evaluation of the spectrum-images are presented in the supplementary materials. FFT and IFFT is performed for analysis for different metal oxide species forming in the coating process of IWI. An example analysis of different metal oxide phases in 20% CZCZC is given in figure S11 in the supplementary files. The analysis indicates the formation of different metal oxide phases on the carrier, indicating good metal oxide distribution and multi metal oxide interfaces and catalyst carrier boundaries, which have been shown to act as active centers in $H_2$- and $CO_2$-adsorption [60,61].

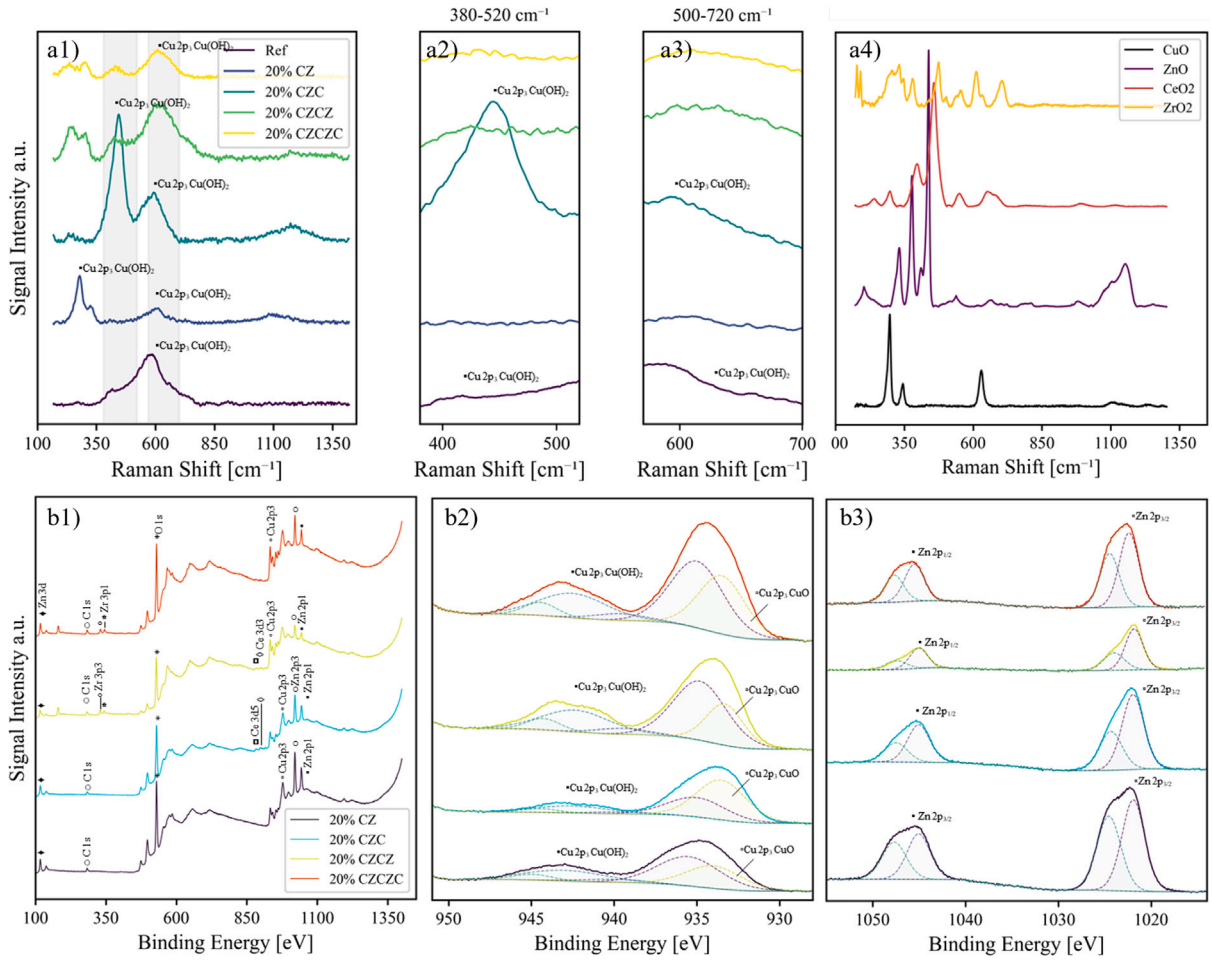


**Fig. 3.** Raman and XPS surface characterization of the catalyst samples: (a1–a3) Raman surveys for 100–1350 $cm^{-1}$ shift (a1) and for 380–520 $cm^{-1}$ (a2) and 500–720 $cm^{-1}$ shift respectively (a3). Reference Raman-spectra for the individual metal oxides used in the infiltration composites (a4). (b1–b3) XPS survey spectrum for all four infiltration composite catalysts (b1). Detailed spectra for 950–930 eV (b2 - CuO) and 1060–1010 eV (b3 - ZnO)

Fig. 3 (a1–a3) shows Raman spectra of the unreduced catalyst surfaces for all promoted carrier samples and the reference sample, as well as reference spectra for all applied metal oxide compounds except CaO [62] The reference CZA catalyst shows a compounded peak, which is dominated by Cu2p at around 600 $cm^{-1}$. All carrier samples show both peaks for $Cu2p_3$ at 300 and 600 $cm^{-1}$ except for 20% CZC, where the spectrum is dominated by large peak at 450 $cm^{-1}$, which is attributed to ZnO and $CeO_2$ forming a compounded overlapping peak, which is significantly less pronounced in all other samples. As is expected, 20% CZCZ and 20% CZCZC show the most diffuse shift patterns, with more metal oxide interacting in spectral measurements. Nonetheless, Cu2p3 is clearly distinguishable in all samples. To further identify the chemical states of metals on the catalyst surfaces and possible effects the promotional steps have on surface CuO and ZnO, we performed XPS analysis for each of the multi metal oxide catalyst samples. XPS spectra of the unreduced sample surfaces are given in Fig. 3 (d). The survey spectrum exhibits all expected peaks, with O1s being most pronounced in 20% CZCZC. The O1s peak is located at 530 eV, which indicates that the detected O-species are bound in fully oxidized metal oxide matrices [63]. The C(1s) signals are most likely caused by the absorption of organic carbon contaminants.

Detail plots for Cu2p and for Zn2p are additionally observed, to identify the effect additional promotion of the catalyst complexes may have on the chemical state of the highly active ZnO and CuO species on the catalyst surfaces. Cu2p can be fitted to two distinctive gaussian curves for $Cu^0$ and $Cu^{2+}$. All catalyst show similar amounts of $Cu^0$ and $Cu^{2+}$, with 20% CZC showing higher availability of $Cu^0$ and 20% CZCZ and 20% CZCZC showing slightly higher contents of $Cu^{2+}$ in comparison. $Cu^0$ has been shown to act as an active center for dissociative $H_2$ adsorption in CuO-based catalyst [64]. This in turn indicates slightly higher availability of hydrogen active centers in 20% CZC compared to the other samples.

On the other hand, $Cu^{2+}$ has been shown to be reduced by CO, acting as active center for the adsorption and enhancing conversion efficiency in CO-hydrogenation to MeOH [65]. The spectra of Zn2p all show strong spin orbit coupling, with two distinctive peaks exhibiting for Zn-species, both of which are compounded. Pure ZnO usually shows two peaks at 1025 eV and 1048 eV, which is most closely reproduced by 20% CZ and 20% CZCZC [66]. The Zn2p peaks of 20% CZ appearing at 1021 eV are compounded with the peak showing at higher binding energy suggesting that identified Zn is present in its $Zn_{2+}$ valence state and the second peak exhibiting at slightly lower binding energy usually being attributed to $Zn_0$ [67]. Through its promotion with $CeO_2$, binding energy of $Zn^0$ shifts downward to around 1020.9 eV. This suggests, that electrons shift to ZnO in metal oxide interaction [68]. This in turn is indicative of more strongly interacted metal oxide activity in 20% CZC and 20% CZCZ, with binding energies in Cu2p also slightly shifted downward. Both Cu2p and Zn2p binding energies shift back upward in 20% CZCZC, which is in line with an enlarged O1s peak, oxygen in metal oxide matrices often acting as electron scavengers in complex metal-metal-oxide interactions [69]. Alternatively, the shift could be explained through other catalyst surface effects such as the formation of defects or fundamental surface restructuring through the

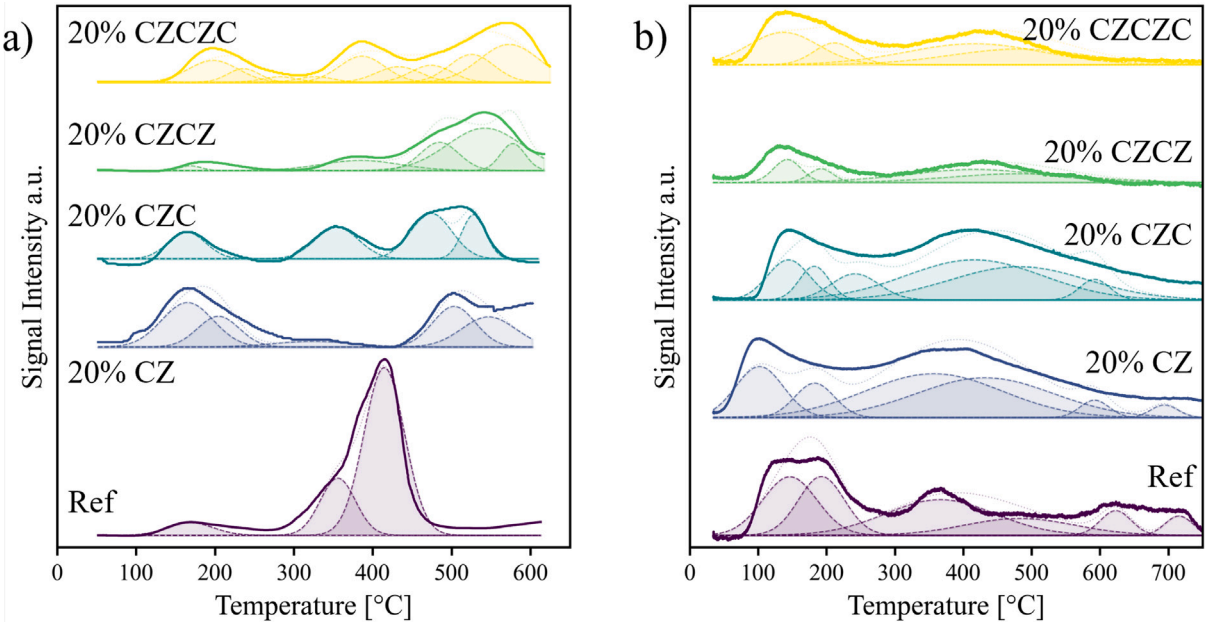


**Fig. 4.** (a) $CO_2$-desorption measurements for the carrier and reference catalysts (b) $H_2$-desorption curves.

addition of further catalyst promoters. The formation of different coordination around Zn and Cu can also be the cause of the observed shift upwards [70].

**Adsorption properties for $CO_2$ and $H_2$**

$H_2$- and $CO_2$-desorption measurement results are given in Fig. 4. The adsorption efficiency of $CO_2$ is, among other factors, dependent on the surface basicity of the catalyst samples [61]. Herein, the carrier-samples all present three compounded desorption peaks, representing weak, medium, and strong basic sites on the surface [71]. The weakest site, with desorption starting at around 100 °C, is associated with the hydroxy group [71]. This seems to be the most relevant basic active site, considering the temperatures usually associated with industrial MeOH synthesis [61,72].

Additionally, $CO_2$ adsorbed in weak basic sites has been shown to facilitate the formation of formate species, which represents the most commonly referred to intermediate in the efficient conversion of $CO_2$ to MeOH [73]. 20% CZ presents the most prominent weak basic site desorption peak. CZA-promotion through 20% CZC and 20% CZCZ reduces peak area under 300 °C, indicating that the addition of $CeO_2$ and $ZrO_2$ strengthens these sites, with the weak basic sites being nearly entirely inhibited through the addition of $ZrO_2$ and the peaks shifting to more strongly interacted sites at higher desorption temperatures. CaO presents strengthened basic sites for the entire range, confirming the principal assumption that CaO-addition can impact the catalyst surface basicity and therefore improve the catalysts ability to adsorb $CO_2$, thus optimizing conversion potential. The measurements also confirm previous studies' findings, in that CaO seems to improve high temperature adsorption properties of catalyst, with 20% CZCZC showing high peak ares over 350 °C. The reference catalyst presents a single, large, compounded desorption peak above 300 °C associated with monodentate carbonates stemming from oxygen-anions of low-coordination, which are less relevant to $CO_2$ adsorption under the herein tested reaction conditions [73]. All carrier catalysts present an additional, high-temperature desorption peak. This peak is also shared with the Ceria-promoted CZA-catalyst sample 20% CZC and with the CaO-added sample 20% CZCZC, although the latter two do not present the desorption peak in the same magnitude as the reference.

Results for quantitative analysis of $CO_2$-desorption properties are given in Table 3. The reference CZA catalyst shows the highest total adsorption amount, with catalytically active mass higher five-fold in contrast. From the promoted catalysts, the $ZrO_2$-$CeO_2$-sample performs the best, adsorbing 23.6 µmol $CO_2$ per gram of total catalyst weight. Maximum desorption peak temperature is highest for 20% CZCZC, indicating that $CO_2$ is most stably adsorbed on the CaO promoted sample.

All carrier catalysts exhibit two distinct desorption peaks for hydrogen-desorption with desorption spanning a significant temperature range from about 30 °C to about 720 °C. The first, lower temperature desorption peak starting significantly below 100 °C for all catalyst samples can be associated with the desorption of atomic hydrogen bound to Cu-species in the catalysts [74].

This peak decreases through the promotional steps presented for the samples in this work, strongly correlating to the overall Cu-content of the samples. The second desorption peak indicates more strongly interacted $H_2$. This peak is very broad and strongly compounded for all herein tested samples, indicating wide dispersion and varying interaction of the associated active sites in the catalyst samples [75]. The reference catalyst is the only investigated sample, that shows a less distributed desorption peak, with strong $H_2$ desorption between 300 and 400 °C and a small compounded desorption peak at very high temperatures starting at 600 °C. This indicates the more homogeneous formation of $H_2$ acting points in the reference sample. The more strongly interacted $H_2$ can be attributed to several different active centers for $H_2$ adsorption, which are partially attributed to bulk Cu or to partially reduced ZnO, where dissociative adsorption of $H_2$ can be assumed [74]. This is in line with the decreasing Cu- and Zn-content in the promoted catalysts, which show reduced desorption peak area compared to the binary 20% CZ carrier catalyst sample. From $H_2$-TPD measurements, metallic copper surface area was determined for the desorption behavior between 300 and 620 K. The results for the determination of reduced copper surface area for the herein presented catalyst samples as well as the reference CZA catalyst are given in Table 4. Desorbed amounts of $H_2$ are high, but generally in line with other recent related studies [12,33]. Metallic copper surface area after reduction is highest for 20% CZ and 20% CZC, with 20% CZCZ showing an unusual dip over adsorption activity for $H_2$. This shows the benefits of IWI-coated catalyst spheres, enabling high surface coverage and over all good accessibility of metallic copper species on the catalyst surface, even surpassing the commercial CZA-reduced copper surface area. High metallic copper surface area in 20% CZC is attributed to $CeO_2$s ability to enhance Cu-dispersion in metal-oxide surface interaction [76].

**Table 3**
$CO_2$-TPD analysis results for supported copper catalysts. Catalyst masses for 20% CZ - 20% CZCZC are reduced to weight of coating (20% of total catalyst weight).

| Sample | Sample mass (g) | Total $CO_2$ (µmol) | Total $CO_2$ (µg) | $CO_2$ per g catalyst (µmol/g) | $CO_2$ per g catalyst (µg/g) | Peak T (° C) |
|---|---|---|---|---|---|---|
| REF | 0.6600 | 12.34 | 542.98 | 18.69 | 822.70 | 415.2 |
| 20% CZ | 0.1160 | 1.58 | 69.50 | 13.61 | 599.15 | 504.5 |
| 20% CZC | 0.1200 | 1.68 | 74.01 | 14.01 | 616.77 | 512.9 |
| 20% CZCZ | 0.1060 | 2.36 | 103.81 | 22.25 | 979.30 | 539.4 |
| 20% CZCZC | 0.1100 | 1.45 | 63.91 | 13.20 | 581.02 | 561.9 |

**Table 4**
$H_2$-TPD results and derived parameters for the catalyst samples.

| Sample | Mass (g) | Cu (wt%) | $H_2$ des. (µmol) | Cu sites/g cat. (µmol/g) | Cu area/g cat. ($m^2$/g) | BET area [11] ($m^2$/g) | Dispersion (–) | Particle size (nm) |
|---|---|---|---|---|---|---|---|---|
| REF | 0.167 | 45.3 | 21.3 | 127.5 | 5.22 | 76 | 0.018 | 58.1 |
| 20% CZ | 0.104 | 11.5 | 53.5 | 516.5 | 21.16 | 132 | 0.285 | 3.6 |
| 20% CZC | 0.114 | 9.3 | 61.2 | 536.5 | 21.98 | 122 | 0.367 | 2.8 |
| 20% CZCZ | 0.174 | 7.8 | 14.2 | 81.9 | 3.36 | 129 | 0.067 | 15.5 |
| 20% CZCZC | 0.128 | 7.5 | 19.8 | 155.2 | 6.36 | 125 | 0.132 | 7.9 |

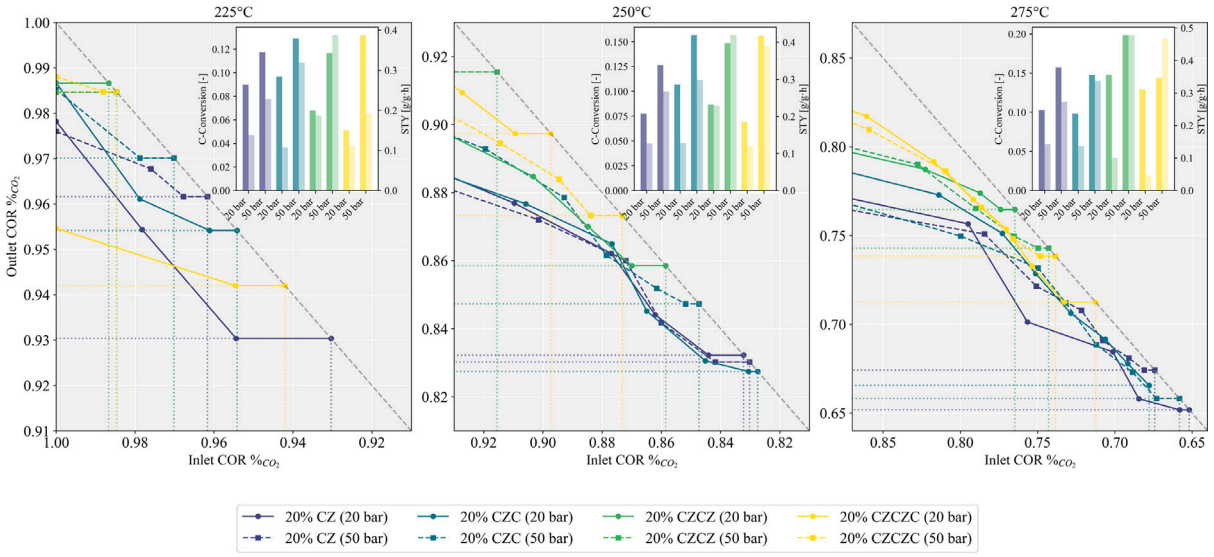


**Fig. 5.** Conversion-equilibria of the presented catalyst samples at 225 °C, 250 °C and 275 °C as well as performance figures for the determined conversion equilibria at 20 bar and 50 bar reactor pressure.

Additionally BET surface area of the samples is used for determination of average particle size and theoretical carrier utilization area [11]. Average particle size is small (3.6 and 2.8 nm) for 20% CZ and 20% CZC with particle sizes assuming much larger values for 20% CZCZ. This does not correlate with the assumption, that high particle dispersion leads to enhanced conversion of carbon oxides, as 20% CZCZ performs the highest conversion rations and STY of the herein samples [48]. This must be attributed to multi-metal-oxide effects in $CO_2$-catalysis, which counteract particle sizes and enhance conversion over 20% CZCZ significantly [18].

### *3.2. Catalyst performance in mixed carbon-oxide synthesis gas*

#### Carbon-conversion equilibria over the promoted carrier catalyst samples

In industrial catalyst application, SynGas streams will be recycled for most commercial MeOH-applications. Even in process applications based upon the direct conversion of $CO_2$ to MeOH, gas compositions inside the synthesis gas loop will therefore contain a mixture of $CO_2$, CO and $H_2$. Applying high recycle ratios in reduced $X_C$-applications for regenerative MeOH-synthesis, the gas composition inside the synthesis loop will gradually develop towards a steady state, where the mixed synthesis gas containing fresh synthesis gas and recycled process gas injected into the reactor will assume a gas composition close to the conversion equilibrium of CO and $CO_2$ towards MeOH, $H_2O$ and CO through RWGS. The conversion efficiency in this steady state is therefore a valuable measure for the catalyst performance under industrial conditions. The development of the influent–effluent COR for all carrier catalyst samples is plotted in Fig. 5. The respective curves end in COR-equilibria, where reactant COR equals effluent COR, indicating conversion equilibrium of both $CO_2$ and CO. Additionally, performance evaluations for the determined equilibria are given for each tested temperature.

As is expected, higher reactor temperatures generally lead to a higher conversion rate of $CO_2$ to CO via RWGS. This leads to effluent COR being lower at high temperatures across all tested pressures for the catalyst samples. It is notable, that 20% CZ exhibits the highest RWGS reaction rates of all carrier catalysts, with reaction equilibrium being reached at 93%$_{vol}$ $CO_2$ at 225 °C, 83%$_{vol}$ at 250 °C and 66%$_{vol}$ at 275 °C reactor temperatures for a set reactor pressure of 20 bar. 20% CZCZ generally exhibits the lowest CO-production rates across the tested temperature and pressure ranges, with 99%$_{vol}$ $CO_2$ for the reaction equilibrium at 225 °C and 20 bar reaction pressure, barely

**Table 5**
Comparison of catalyst performance with selected literature values.

| Catalyst | COR | SN | T (° C) | p (bar) | $X_C$ (%) | Source |
|---|---|---|---|---|---|---|
| CZA (ref) | 0.71 | 3.0 | 250 | 50 | 39.1 | This work |
| $CuZnO/Al_2O_3$ | 0.71 | 3.0 | 250 | 50 | 17.5 | This work |
| $CuZnOCeO_2/Al_2O_3$ | 0.71 | 3.0 | 250 | 50 | 18.9 | This work |
| $CuZnOCeO_2ZrO_2/Al_2O_3$ | 0.71 | 3.0 | 250 | 50 | 21.8 | This work |
| $CuZnOCeO_2ZrO_2CaO/Al_2O_3$ | 0.71 | 3.0 | 250 | 50 | 26.5 | This work |
| $Cu/Al_2O_3$ | 0.83 | 6.5 | 225 | 20 | 12.1 | [10] |
| $Cu/TiO_2$ | 0.83 | 6.5 | 225 | 20 | 10.0 | [10] |
| Raney Cu | 0.83 | 6.5 | 225 | 20 | 8.1 | [10] |
| $Cu/CeO_2$ | 0.75 | 2.0 | 250 | 30 | 5.5 (calc) | [12] |
| $Pd/ZrO_2$ | 0.80 | 2.25 | 200 | 50 | 6.0 | [15] |
| $Pd/CeO_2ZrO_2$ | 0.80 | 2.25 | 200 | 50 | 7.0 | [15] |
| $CuCeO_2/ZrO_2$ | 1.00 | 2.0 | 260 | 30 | 20.5 | [31] |
| $ZnO–ZrO_2$ | 0.50 | 2.0 | 240 | 50 | 7.8 | [77] |
| $CuCeO_2ZrO_2$ | 1.00 | 2.0 | 280 | 30 | 10.5 | [78] |
| CuZnO | 0.67 | 2.0 | 230 | 40 | 8.0 | [79] |
| CuZnO-MLa | 0.27 | 2.0 | 240 | 30 | 22.6 | [80] |
| $Cu/ZnO/Al_2O_3$ | 0.50 | 2.0 | 230 | 30 | 10.0 (calc) | [81] |
| Cu/MgO | 0.57 | 2.0 | 230 | 30 | 0.6 (calc) | [81] |
| Cu/ZnO | 1.0 | 2.0 | 230 | 20 | 5.5 | [82] |
| CuMgO/ZSM | 0.13 | 4.0 | 210 | 30 | 21.4 (calc) | [83] |
| CZA-MgO | 0.16 | 2.5 | 240 | 30 | 12.0 | [84] |
| $CZA-ZrO_2$ | 0.16 | 2.5 | 240 | 30 | 23.2 | [84] |
| $CuMgOCeO_2$ | 0.14 | 1.9 | 240 | 50 | 50.7 | [85] |
| $Cu/Ce_{0.2}Zr_{0.8}O_2$ | 1.00 | 2.0 | 280 | 30 | 5.7 | [86] |
| $Cu/ZnO/ZrO_2CeO_2$ | 1.00 | 2.0 | 230 | 30 | 22.8 | [87] |
| $Cu/CeZrO_2$-MO | 1.00 | 2.0 | 240 | 30 | 4.7 | [88] |
| $CuZnOZrO_2$ | 1.00 | 2.0 | 240 | 30 | 17.4 | [89] |
| $CuCeO_2/TiO_2$ | 1.00 | 2.0 | 260 | 8 | 1.8 | [90] |
| $CuCeO_2/SiO_2$ | 1.00 | 2.0 | 260 | 8 | 3.8 | [90] |
| CZA-Th | 0.25 | 2.0 | 225 | 40 | 44.5 | [91] |
| CrPd/ZnO | 0.25 | 2.0 | 325 | 51 | 20.0 (calc) | [92] |
| $CuZnOGa_2O$ | 1.0 | 1.8 | 240 | 40 | 27.0 | [93] |

shifting any of the introduced $CO_2$ to CO. This is also reflected in the determined performance at reaction equilibrium, with 20% CZCZ showing the highest $STY_{MeOH}$ across the tested temperature and pressure ranges for its respective conversion equilibria, highlighting the effectiveness of $ZrO_2$ and $CeO_2$ as promoters in CuO/ZnO MeOH-catalysts. This is also inline with comparable studies, that have investigated multiple-component catalysts for the direct conversion of $CO_2$ to MeOH, with $ZrO_2$ and $CeO_2$ being able to significantly improve intermediate stability and facilitate conclusive conversion without premature desorption of CO as reaction intermediate [18,28,72]. Comparing the individual reaction equilibria, highest $STY_{MeOH}$ of 0.47 $g_{MeOH}/(g_{Cat}h)$ is reached by 20% CZCZ at 275 °C reactor temperature and 50 bar reaction pressure.

Catalyst performance in mixed carbon oxide synthesis gas conditions (COR = 0.71) is additionally correlated to the results of $CO_2$-adsorptions properties and metallic Cu surface area derived from $H_2$-TPD. Results are given in Fig. 6. Astonishingly, Cu-surface area shows inversely proportional correlation to the measured $STY_{MeOH}$ of the catalyst samples. This suggests, that $H_2$ adsorption does not represent an inhibiting factor in the herein tested samples. Considering these results, testing the catalysts exclusively at stoichiometric or super stoichiometric conditions can be seen as a limitation of the presented work, as over supply with $H_2$ might have masked shortcomings in active site $H_2$ coverage for the wash coated catalyst samples. On the other hand, catalyst performance correlates more clearly with $CO_2$-adsorption efficacy, suggesting that effective coverage of all active sites with $CO_2$ plays a more prominent role in ensuring neighboring reactant adsorption and subsequent catalyzed formation of MeOH or its intermediates. Nonetheless, the reference precipitated catalyst performs the best, with both the highest specific copper surface area and the highest capacity for $CO_2$-adsorption.

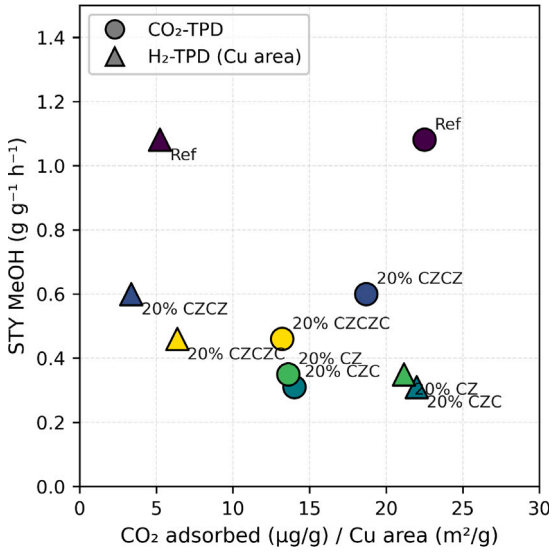


**Fig. 6.** Correlation of metallic Cu surface area and $CO_2$-adsorption properties to catalyst performance measured at COR = 0.71, p = 50 bar, $T$ = 250 °C and GHSV = 10,000 $h^{-1}$.

**Catalyst performance across varied COR**

For performance evaluation of the samples and as basis for the parameter optimization of the later presented kinetic reaction model for each of the catalyst samples, a more comprehensive catalyst screening was conducted using different influent COR compositions for different reaction pressures, temperatures and GSHV. To ensure hydrogen coverage of the samples and to be able to eliminate insufficient hydrogen coverage as a factor in kinetic analysis and performance evaluation, hydrogen supply was kept super-stoichiometric ($SN$ = 3.0) across all reaction conditions and their individual combinations(see Fig. 7).

As has been reported before for $CO_2$-only reaction conditions, 20% CZCZC shows the highest $X_C$ across all tested gas compositions [11]. However, 20% CZCZ performs slightly better for single reactor pass

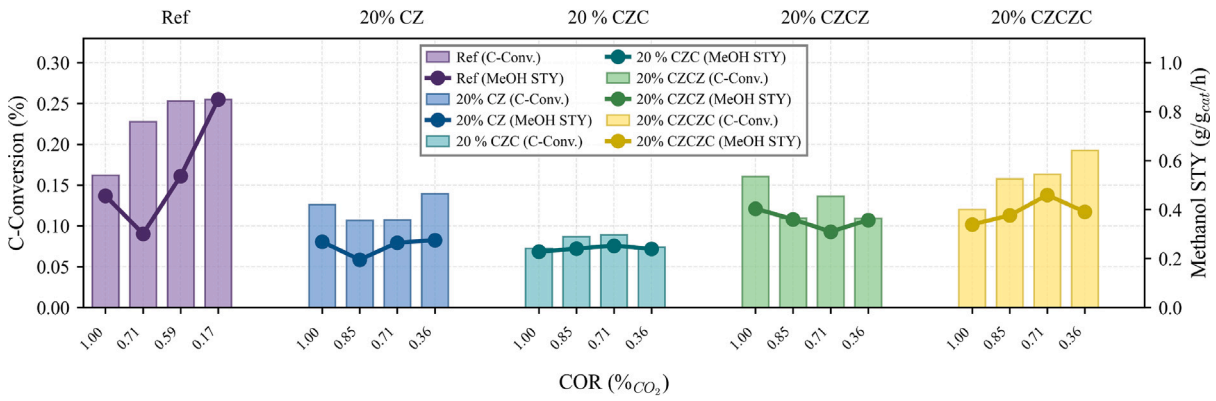


**Fig. 7.** Conversion Performance of the Samples under different COR influent compositions (35 bar reactor pressure, 250 °C reactor temperature, 10.000 $h^{-1}$ GHSV)

$STY_{MeOH}$. All catalysts show the overall highest $X_C$ either at reaction conditions containing no CO in the reactant feed gas or at the lowest influent gas COR. High $X_{CO_2}$ at high COR can easily be attributed to the partial conversion of $CO_2$ to CO through RWGS. By implication, high $STY_{MeOH}$ at low COR can be attributed to good direct conversion of CO to MeOH, with the lower $CO_2$-content in synthesis gas causing less CO-byproduction and more of the available carbon being converted directly to MeOH. The high selectivity of 20% CZCZ under $CO_2$-only synthesis conditions with lower conversion and higher $STY_{MeOH}$ cannot be explained at this point, as it contradicts the otherwise uniform correlation between $X_C$ and $STY_{MeOH}$. Highest overall tested $X_C$ and $STY_{MeOH}$ are reached by the industrial reference catalyst at low COR and high pressure, as is common in industrial applications of the used catalyst sample.

The results shown in Table 5 indicate that the coated CZA-based samples examined here, exhibit $X_C$ levels that are within the same general range as those reported for Cu-based systems tested under comparable temperatures and pressures. Notably, the CZA reference catalyst achieved 39.1% carbon conversion at 250 °C and 50 bar, which substantially exceeds the performance of most literature catalysts tested under less demanding conditions. Nonetheless, the coated carrier samples perform well in comparison to recent literature. For instance, $Cu/Al_2O_3$ and $Cu/TiO_2$ systems reported by Nielsen (12.1% and 10.0% respectively) were tested at only 225 °C and 20 bar and underperformed the present work by factors of 3.2×and 3.9×.

Direct comparison with promoter-modified systems further illustrates the effectiveness of the CZA formulation. CZCZC achieved 26.5% conversion under identical conditions to the reference (250 °C, 50 bar), surpassing the $Cu/CeO_2$ system (5.5%, Zhu et al.) by 4.8×, and substantially outperforming the $Pd/ZrO_2$ and $Pd/CeO_2ZrO_2$ catalysts (6.0% and 7.0%, respectively) despite the latter being tested at significantly higher space velocities. When compared at more similar operating conditions, the present four-component CZA catalyst (26.5%) approaches or even surpasses several literature benchmarks: $CuCeO_2/ZrO_2$ (20.5%, Poto et al. at 260 °C) and $Cu/ZnO/ZrO_2CeO_2$ (22.8%, Ban et al. at 230 °C).

Several aspects appear relevant to understanding the observed performance trends: the geometry and nature of the carrier ($\gamma$-$Al_2O_3$ washcoated spheres), and the composition and application mode of the promoters ($CeO_2$, $ZrO_2$, CaO).

Structured $\gamma$-$Al_2O_3$ supports and thin washcoating are often employed in scale-up or structured catalyst configurations. Such arrangements may allow for reduced metal loading per reactor volume while retaining a high external surface area and potentially beneficial transport characteristics, such as lower macropore diffusion resistance and improved heat transfer [49]. Under these circumstances, thinly coated microspheres can exhibit apparent reaction rates comparable to bulk catalysts despite containing less Cu overall. This leads to over all higher ratios between $X_C/w_{Catalyst}$.

This may partly account for the carbon conversions measured in the present samples, where effective utilization of the active phase and efficient mass transfer could contribute to the achieved high performance. These structural factors might therefore offer particular advantages in systems where process intensification, reduced metal use or fast and simple production of multiple samples using a standardized effective manufacturing protocol are targeted [10].

Differences in promoter chemistry and the mode of their incorporation can also provide additional insight into the performance observed. $CeO_2$ has been reported to enhance $CO_2$ activation through the formation of oxygen-vacancy-related sites, potentially improving $CO_2$ adsorption and facilitating methanol formation within Cu–ZnO frameworks, often associated with somewhat higher selectivity than simple Cu/ZnO systems [12]. Overall, the present CZA-based formulations show the following trend: the $CeO_2$-containing catalyst achieved 18.9% conversion compared to 17.5% for the base $CuZnO/Al_2O_3$ catalyst, demonstrating the promoter's beneficial effect. $ZrO_2$, in contrast, is typically linked to stronger metal–support interactions and the stabilization of dispersed Cu ensembles, which in some cases may help suppress the RWGS reaction and favor methanol production [26]. The incorporation of $ZrO_2$ alongside $CeO_2$ in the present work further improved performance to 21.8%, suggesting synergistic interactions between the two promoters. CaO, as a basic additive, may modify the surface acid–base balance, influencing $CO_2$ adsorption and water inhibition effects. The full four-component system incorporating CaO reached 26.5% conversion, indicating that this basic additive provides incremental performance enhancement. This hierarchical performance trend ($CeO_2$ alone: +1.4% absolute; $CeO_2$ + $ZrO_2$: +4.3% absolute; $CeO_2$ + $ZrO_2$ + CaO: +9.0% absolute relative to baseline) demonstrates the cumulative benefits of each promoter addition. Depending on dispersion and loading, this could shift the relative activity or product distribution observed.

It is also worth noting that literature reports employ these promoters using different synthesis strategies, for example, co-impregnation, physical mixing, core–shell layering, or washcoating. Such distinctions in morphology and texture (surface versus bulk activity) explain part of the variability seen in reported $X_C$ values, even when similar promoter compositions are used. For example, the washcoated $CuZnOCeO_2ZrO_2$ system presented here (21.8%) outperforms the $CuCeO_2ZrO_2$ catalyst reported by Han et al. (10.5% at 280 °C), despite being tested at a lower temperature (250 °C), suggesting that the washcoating approach provides superior mass transfer and active site accessibility. Hence, the comparisons in Table 5 should be viewed as reflecting not only promoter chemistry but the combined effect of structural implementation and local environment [12,26].

**Table 6**
Mass transfer analysis results for the catalyst samples.

| Sample | $CO_2$ | | MeOH | | $H_2O$ | | Mears |
|---|---|---|---|---|---|---|---|
| | $\Phi_{WP}$ (–) | $D_K$ ($\times 10^{-6}$) | $\Phi_{WP}$ (–) | $D_K$ ($\times 10^{-6}$) | $\Phi_{WP}$ (–) | $D_K$ ($\times 10^{-6}$) | (–) |
| 20% CZ | 0.054 | 1.80 | 0.138 | 2.11 | 0.098 | 2.81 | 2.1e–04 |
| 20% CZC | 0.053 | 1.90 | 0.139 | 2.22 | 0.098 | 2.97 | 2.2e–04 |
| 20% CZCZ | 0.060 | 1.92 | 0.128 | 2.25 | 0.091 | 3.00 | 2.3e–04 |
| 20% CZCZC | 0.064 | 1.94 | 0.134 | 2.27 | 0.094 | 3.03 | 2.5e–04 |

Finally, variations in mixed $CO/CO_2$ feed composition (COR) appear to influence $X_C$ dynamics greatly relative to pure $CO_2$ hydrogenation tests. The presence of CO in the feed may affect reaction pathways through altered $CO_2$ activation behavior and a modified balance between RWGS and MeOH synthesis. In addition, CO-rich mixtures may mitigate water accumulation by engaging the WGS equilibrium, potentially reducing inhibition effects at higher conversions. Literature comparisons illustrate that the influence of co-fed CO can either enhance or suppress MeOH formation, depending on COR, pressure, and conversion level [10,77]. Notably, the present work employs a consistent COR of 0.71 across all formulations for comparison, whereas gathered literature comparisons span a wide range (0.13–1.00), making direct performance attribution to promoters, carriers and the interactions thereof challenging. For instance, systems with lower COR values such as CZA-Th (0.25 COR, 44.5% at 225 ° C, 40 bar; Vergara et al.) or $CuMgOCeO_2$ (0.14 COR, 50.7% at 240 °C, 50 bar; Pandey et al.) achieve exceptional conversions, confirming that CO enrichment relative to $CO_2$ may provide additional thermodynamic or kinetic advantages. In this context, the present data, which systematically vary COR under otherwise consistent structural and compositional conditions, provide a coherent baseline for exploration of beneficial interactions noted for each promoter under mixed SynGas environments. Additional performance comparison metrics can be found for $CO_2$-only SynGas streams elsewhere [11].

Concerning the chemical equilibria recorded in this work, CZ shows the lowest COR for equilibrium conversion at approx. 0.83 for 250 °C reactor temperature, requiring the highest amounts of CO in the reactor make up gas for balanced reactant conversion. This equates to a $CO_2/CO$ ratio of about 4:1, which is considerably higher in comparison to previously reported equilibrium values for CZA catalyst systems, where equilibrium conversion has been reported at COR of 10%–35% [10,53]. This showcases the influence of promoters and support structure on the reaction mechanism and equilibrium. $CeO_2$ and $ZrO_2$ promoters added to Cu/ZnO catalysts strongly enhance $CO_2$ activation and hydrogenation. This is mainly due to their oxygen storage capacity and the stabilization of formate intermediates formed during MeOH synthesis. These promoters shift the reaction equilibrium towards the $CO_2$ hydrogenation pathway, resulting in a lower $CO/CO_2$ ratio required to reach equilibrium conversion [10,40]. The promoters, along with the highly porous alumina support, suppress the CO-hydrogenation pathway relative to the $CO_2$ pathway much more effectively than in unpromoted Cu/ZnO catalysts. This suppression reduces the competitiveness of CO as a reactant, causing equilibrium to be established at lower partial pressures of CO, thus lowering the $CO/CO_2$ ratio at equilibrium. Furthermore, $CeO_2$ and $ZrO_2$ are known to enhance the water-gas shift (WGS) reaction, which converts CO and $H_2O$ to $CO_2$ and $H_2$. This catalytic promotion can enhance conversion of CO to $CO_2$ dynamically increasing the relative concentration of $CO_2$ in the steady state reaction environment. As a result, the $CO/C_2$ ratio at equilibrium is further reduced in the promoted catalyst formulations CZC, CZCZ and CZCZC [12].

### 3.3. Results of the parameter fitting

For parameter fitting, no major mass transfer limitations were assumed on the basis of the extensive test for limitations described above. Table 6 shows average transfer coefficients and Weisz- as well as Mears-parameters for each of the catalysts for $CO_2$, $H_2O$ and MeOH, which are most prone to experience transfer limitations on a molecular level [6]. The reported values were calculated as mean averages from determining the coefficients for every individual test conducted in a first optimization run. A full report of the transfer limitations for every test run is given in the supplementary materials. As can be seen, average Mears criteria are very low on average. External diffusion limitations were therefore excluded from the fitting process. Concerning internal mass transfer limitations, only MeOH shows values above 0.1 for all catalysts. As $H_2$, CO, $CO_2$ and $H_2O$ did not show inhibiting mass transfer behavior, and transfer limitation of the MeOH product were limited in most test conditions applied in this study, all transfer limitations were omitted in further parameter optimization.

The parameters fitted to the Graaf-model with the chosen combinations of rate determining steps and some statistical indicators towards model fit are given in Table 7. Additionally, a short list of comparable studies that have refitted the Graaf kinetics to other applications using adapted CZA catalyst formulas is given in Table 8 [31,42,47,94]. The reported studies underline the meaningfulness of the calculated values from the herein tested catalyst samples, with activation energies lower — following reduced activity of the reported samples compared to the industrial CZA catalyst.

As reported by Graaf et al. and many other recent studies investigating the kinetics of MeOH-synthesis over CuO / ZnO-based catalyst formulas, the optimization performed in this work yields the mathematical exclusion of the formation of MeOH through hydrogenation of CO [10,31,42,46,47]. This is represented by the fact, that calculated rates for CO-hydrogenation assume near zero values in reactor calculation based upon the herein presented models. CO-hydrogenation can thus be neglected in future analysis of the model fit presented in this work. Nonetheless, the model combination given in Table 8 shows the optimized full model combination, including step A — CO-hydrogenation, for comparability to related studies. Here, the chosen optimized rate-determining step changes from one promotional step to another, with the fit minimizing CO-hydrogenation depending on the test results.

For the binary CuO/ZnO carrier catalyst, the optimization yields the best combination of models for the A3B2C3 model, which is also kinetically chosen by Graaf et al. for their model presented for the industrial catalyst using the same active phases. Promotion of the binary catalyst changes the rate determining steps, with $CeO_2$-addition altering the rate determining step for MeOH-generation through $CO_2$-hydrogenation, which is expectable on a molecular level, as $CeO_2$ is able to produce active centers for $CO_2$-adsorption that differ from those usually assumed to be active in CZA [20]. Here, initial hydrogenation of adsorbed $CO_2$ towards HCOO in the formate pathway is favored by the $CeO_2$ promoted catalyst sample over the hydrogenation of $H_2COO$, as initially shown in the original model by Graaf et al.. Consideration of $H_2COO$-hydrogenation as rate determining step is supported by literature in CZA-catalysts as well as in $ZrO_2$ and $CeO_2$-containing formulas [31]. $ZrO_2$-promotion changes the rate determining step of both RWGS and $CO_2$-hydrogenation mathematically again, with RDS in $CO_2$-hydrogenation returning to initial COO-hydrogenation and the RDS for RWGS switching from HCOO-hydrogenation towards $H_2O$ and CO to initial COO-hydrogenation to HCOO. CaO-promotion in

**Table 7**
Kinetic parameters for novel 20% catalyst systems.

| | 20% CZ | 20% CZC | 20% CZCZ | 20% CZCZC |
|---|---|---|---|---|
| Model | A3B2C3 | A3B2C1 | A2B1C3 | A4B1C3 |
| Rate Constants: $k = A \times e^{-E_a/RT}$ | | | | |
| $A_{MeOH,CO}$ | 1.18 | 32.1 | 8.21 | 0.21 |
| $E_{a,MeOH,CO}$ (kJ/mol) | 8.02 | 3.20 | 1.32 | 85.21 |
| $A_{MeOH,CO_2}$ | $3.76 \times 10^{7}$ | $3.20 \times 10^{8}$ | $6.34 \times 10^{10}$ | $5.44 \times 10^{3}$ |
| $E_{a,MeOH,CO_2}$ (kJ/mol) | 79.3 | 67.5 | 130.8 | 130.8 |
| $A_{RWGS}$ | 0.672 | 1.37 | 0.27 | $1.12 \times 10^{-2}$ |
| $E_{a,RWGS}$ (kJ/mol) | 27.5 | 8.46 | 25.2 | 29.4 |
| Adsorption Constants: $K = B \times e^{\Delta H/RT}$ | | | | |
| $B_{CO}$ | $1.00 \times 10^{-5}$ | $1.55 \times 10^{-2}$ | $1.36 \times 10^{-2}$ | $1.12 \times 10^{-2}$ |
| $\Delta H_{CO}$ (kJ/mol) | 33.8 | 4.38 | 29.7 | 1.01 |
| $B_{CO_2}$ | $2.91 \times 10^{-7}$ | $3.79 \times 10^{-7}$ | $1.70 \times 10^{-11}$ | $5.02 \times 10^{-8}$ |
| $\Delta H_{CO_2}$ (kJ/mol) | 57.4 | 30.0 | 114.3 | 66.8 |
| $B_{H_2O}$ | $7.07 \times 10^{-12}$ | $1.33 \times 10^{-11}$ | $7.48 \times 10^{-14}$ | $1.21 \times 10^{-13}$ |
| $\Delta H_{H_2O}$ (kJ/mol) | 125.7 | 131.9 | 137.0 | 124.9 |
| *$H_2$: Parameters compounded with $H_2O$* | | | | |
| *statistical agreement of the models predicted values with the measured data* | | | | |
| $R^2$ $CO_2$ () | 0.91 | 0.99 | 0.95 | 0.98 |
| $R^2$ CO () | 0.97 | 0.97 | 0.92 | 0.93 |
| $R^2$ MeOH () | 0.87 | 0.91 | 0.94 | 0.93 |
| $R^2$ $H_2O$ () | 0.97 | 0.92 | 0.91 | 0.91 |
| MAPE MeOH (%) | 11.56 | 10.11 | 15.38 | 16.51 |
| MAPE $H_2O$ (%) | 9.21 | 8.41 | 11.12 | 11.76 |
| CCC MeOH | 0.85 | 0.94 | 0.81 | 0.83 |
| CCC $H_2O$ | 0.91 | 0.96 | 0.84 | 0.82 |

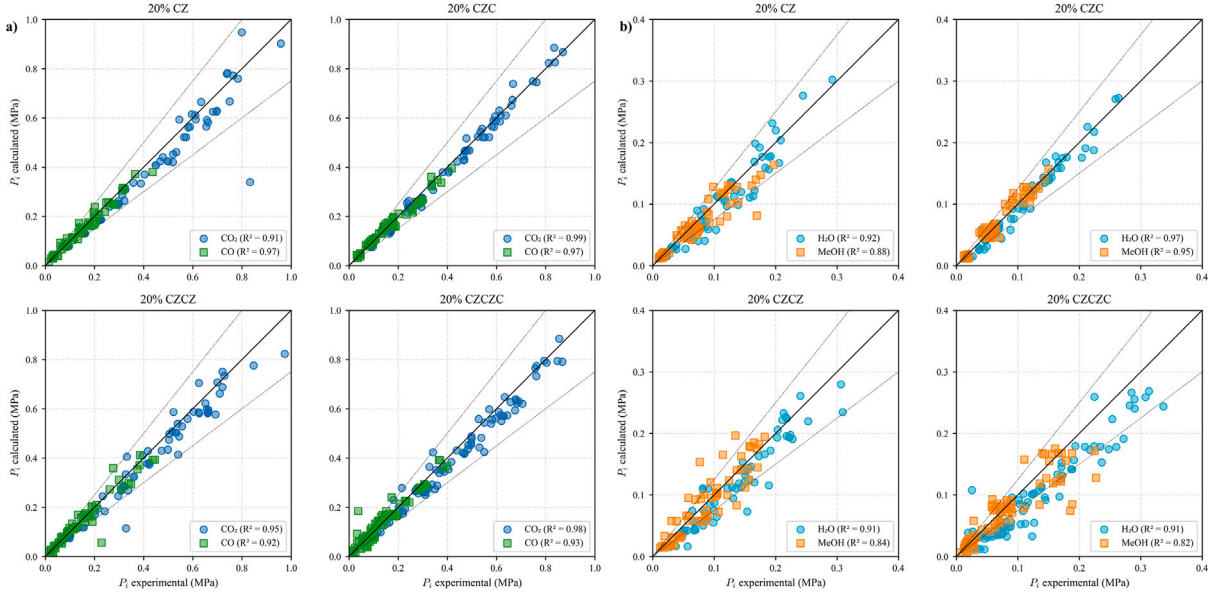


**Fig. 8.** Parity Plots for measured vs. predicted effluent partial pressures for (a) CO and $CO_2$ and (b) MeOH and $H_2O$ in the four catalyst samples.

the quinary 20% CZCZC catalyst sample does not further alter the mathematical composition of the overall model, retaining the RDS shown for 20% CZCZ, while exhibiting slightly reduced activity towards $CO_2$-conversion towards MeOH.

The values fitted to the Graaf-model in this work assume parameter ranges that are comparable to values from similar parametrization works. On the one hand, this confirms the applicability of the presented fitting procedure, utilizing a multi initial parameter fit. In further discussion of the results, this could on the other hand also be attributed to the published optimization algorithm finding local minima close to the initial guesses taken from literature, thus providing a globally sub-optimal fit within close numerical proximity of the initial guess. Nonetheless, the models perform well in predicting CO- and $CO_2$ conversion as well as MeOH and $H_2O$-production in the test reactor, showing high overall agreement with the measured data. Key statistical indicators are given alongside the optimized fitting parameters in Table 7. $R^2$ of calculated CO, $CO_2$ and MeOH reactor exit partial pressures as well as MAPE and CCC of MeOH reactor exit partial pressures are shown for demonstration of model fit quality and for comparison of different approaches for statistical evaluation of modeling results. In general, the model for 20% CZC shows the best fit statistically, with $R^2$ for all species above 0.91 and a Mean Absolute Percentage Error (MAPE) for MeOH formation of approx. 10%, implying an average

**Table 8**
Kinetic parameters for methanol synthesis catalysts.

| | Graaf et al. [47] | Nestler et al. [42] | Poto et al. [31] | Slotboom et al. [94] |
|---|---|---|---|---|
| Catalyst Information | | | | |
| Catalyst | $CuO/ZnO/Al_2O_3$ | $CuO/ZnO/Al_2O_3$ | $CuO/ZnO/CeO_2/ZrO_2$ | $CuO/ZnO/Al_2O_3$ |
| Manufacturer | Haldor Topsoe | Clariant | – | – |
| Type | Coprecipitation | Coprecipitation | Coprecipitation | Different data sets |
| Model | 323 | 323 | 313 | – |
| Rate Constants: $k = A \times e^{-E_a/RT}$ | | | | |
| $A_{MeOH,CO}$ | $2.69 \times 10^7$ | – | $7.103 \times 10^{-1}$ | – |
| $E_{a,MeOH,CO}$ (kJ/mol) | 109.9 | – | 33.8 | – |
| $A_{RWGS}$ | $7.31 \times 10^8$ | 244.43 | $2.765 \times 10^{11}$ | $1.111 \times 10^{10}$ |
| $E_{a,RWGS}$ (kJ/mol) | 123.4 | 53.7 | 13.4 | 203.0 |
| $A_{MeOH,CO_2}$ | $4.36 \times 10^2$ | $2.356 \times 10^{-5}$ | $1.416 \times 10^9$ | $7.414 \times 10^{14}$ |
| $E_{a,MeOH,CO_2}$ (kJ/mol) | 65.2 | 14.7 | 12.0 | 166.0 |
| Adsorption Constants: $K = B \times e^{\Delta H/RT}$ | | | | |
| $B_{CO}$ | $7.99 \times 10^{-7}$ | $1.44 \times 10^{-17}$ | $3.561 \times 10^{-3}$ | – |
| $\Delta H_{CO}$ (kJ/mol) | 58.1 | −0.57 | −8.44 | – |
| $B_{CO_2}$ | $1.02 \times 10^{-7}$ | $4.223 \times 10^{-6}$ | $6.173 \times 10^{-7}$ | – |
| $\Delta H_{CO_2}$ (kJ/mol) | 67.4 | 0 | 56.7 | – |
| $B_{H_2O}$ | $4.13 \times 10^{-11}$ | $6.407 \times 10^{-13}$ | $3.521 \times 10^{-12}$ | $126.4 \pm 66$ |
| $\Delta H_{H_2O}$ (kJ/mol) | 104.5 | 126.8 | 124.2 | – |
| $H_2$: *Parameters compounded (Slotboom:* $K_{H_2} = 1.099 \pm 0.66$*)* | | | | |

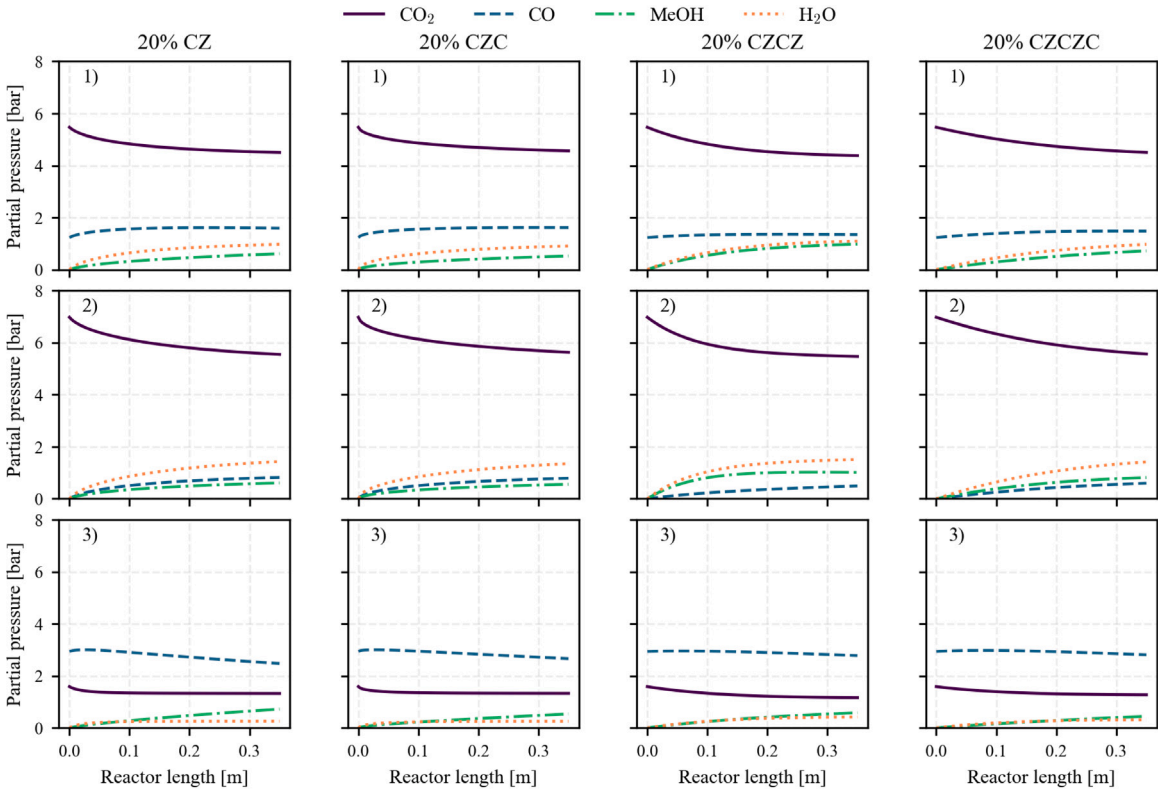


**Fig. 9.** Calculated concentration profiles inside the test reactor for three different inlet gas compositions. Top to bottom: (1) COR = 0.81, SN = 3; (2) COR = 1, SN = 3; (3) COR = 0.36, SN = 3.

deviation of calculated values for MeOH formation of only 10% compared to the measured test data. The fitted models for 20% CZCZ and 20% CZCZC show slightly inferior statistical agreement with the measured data, but still perform well with $R^2$ for all species except for $H_2O$ above 0.9 and MAPE of approx. 15% concerning prediction efficacy towards MeOH formation. It can be argued that increased promotion of the CZA formulation alters the mechanisms of MeOH, CO, and $H_2O$ formation more substantially, making the original assumption by Graaf et al. less applicable to the highly promoted samples and therefore leading to a slightly reduced model fit quality. Calculated $H_2O$ formation shows the lowest agreement with test data for all catalysts. This is attributed to condensation losses in the test apparatus and generally less unambiguous calibration results for GC-calibration towards $H_2O$ in the gas phase. Fig. 8 shows the parity plots of CO- and $CO_2$- (a) as well as MeOH and $H_2O$- (b) reactor exit partial pressures with 25% deviation bandwidth marked inside the sub-plots. As can

**Table 9**
Normalized sensitivity of key model outputs towards the variation of selected model parameters. Sensitivity is given as compounded value for first order single parameters impact and higher order cross sensitivities.

| Model factor | $r_{MeOH}$ | $X_{CO2}$ | $r_{H2O}$ | $S_{MeOH}$ |
|---|---|---|---|---|
| **20% CZ** | | | | |
| $A_{MeOH,CO_2}$ | 0.2720 | 0.2313 | 0.2313 | 0.0910 |
| $E_{a,RWGS}$ | 0.0093 | 0.4626 | 0.4626 | 0.3553 |
| $B_{CO_2}$ | 0.2719 | 0.1861 | 0.1861 | 0.1258 |
| $\Delta H_{CO_2}$ | 3.0409 | 1.8258 | 1.8258 | 1.4235 |
| $B_{H_2O}$ | 0.2747 | 0.1941 | 0.1941 | 0.1262 |
| **20% CZC** | | | | |
| $A_{MeOH,CO_2}$ | 0.2720 | 0.2313 | 0.2313 | 0.0910 |
| $A_{RWGS}$ | 0.0039 | 0.0406 | 0.0406 | 0.0355 |
| $B_{CO_2}$ | 0.2719 | 0.1861 | 0.1861 | 0.1258 |
| $\Delta H_{CO_2}$ | 3.0409 | 1.8258 | 1.8258 | 1.4235 |
| $B_{H_2O}$ | 0.2747 | 0.1941 | 0.1941 | 0.1262 |
| **20% CZCZ** | | | | |
| $A_{MeOH,CO_2}$ | 0.0038 | 0.0004 | 0.0004 | 0.0035 |
| $A_{RWGS}$ | 0.0064 | 0.0030 | 0.0030 | 0.0088 |
| $B_{CO_2}$ | 0.0008 | 0.0002 | 0.0002 | 0.0010 |
| $\Delta H_{CO_2}$ | 0.0068 | 0.0018 | 0.0018 | 0.0082 |
| $B_{H_2O}$ | 0.0000 | 0.0000 | 0.0000 | 0.0000 |
| **20% CZCZC** | | | | |
| $A_{MeOH,CO_2}$ | 0.0038 | 0.0004 | 0.0004 | 0.0035 |
| $A_{RWGS}$ | 0.0064 | 0.0030 | 0.0030 | 0.0088 |
| $B_{CO_2}$ | 0.0008 | 0.0002 | 0.0002 | 0.0010 |
| $\Delta H_{CO_2}$ | 0.0068 | 0.0018 | 0.0018 | 0.0082 |
| $B_{H_2O}$ | 0.0000 | 0.0000 | 0.0000 | 0.0000 |

be seen, the fitted model for 20% CZC performs very well, with no estimation outliers outside of the 25% deviation areas. The 20% CZC model is able to accurately predict CO and $CO_2$ conversion as well as CO formation in RWGS to an $R^2$ of 0.99, demonstrating both the quality of the fitting procedure as well as underlining the quality of Graaf model in applications of parameter refitting for adapted MeOH-catalyst studies. Estimation of the 20% CZCZ model shows the most disarranged parity image, with single outliers being located considerably outside the 25% boundaries. For $H_2O$ and MeOH, as with CO and $CO_2$ reactor exit pressures, 20% CZC shows the best statistical model fit towards the experimental data. All models show $R^2$ higher than 0.8 for predicting MeOH-effluent molar fractions and $R^2$ above 0.9 for $H_2O$ production. Grave prediction outliers are attributed to testing inaccuracies. Model accuracy for predicting MeOH and $H_2O$ production is significantly lower than for the calculation of carbon-oxide conversion. This is in line with multiple other recent studies and can be attributed to several factors in testing and model optimization, of which product retention in the gas probing system and enhanced measurement variance in GC calibration for liquid products are two possible reasons [42,44].

The parametrized models for each catalyst are also tested for their performance in calculating concentration gradients in real world reactor setups. For this, the previously introduced quasi-isothermal reactor model is applied. The conversion gradients inside the reactor model are probed for each catalyst using gas compositions tested in this work, to investigate the influence each promotional step for the carrier catalysts has on the species evolution inside the reactor along the *z*-axis. Fig. 9 shows the calculated concentration gradients inside the 0.035 m long reactor for three different reactor inlet compositions applying super stoichiometric conditions for COR = 1, COR = 0.81 and COR = 0.36. As can be taken from the subplots, educt consumption and product generation are relatively high in the first third of the reactor. 20% CZ and 20% CZC both exhibit high CO-production in the first third of the reactor, with CO-concentration reaching equilibrium fast and not changing much after about 0.1 m reactor length. Equally, $CO_2$-consumption is high at the beginning of the reactor, slowing down considerably after CO-concentration has reached its equilibrium. Thus, $H_2O$ formation is high at the beginning of the reactor, being reduced as CO-concentration in the reactor reaches its equilibrium, only influenced much by the co-generation of MeOH and $H_2O$ in $CO_2$-hydrogenation towards MeOH afterwards. This is in line with comparable studies, that have probed concentration profiles of the Graaf-model in tubular 1D reactor setups recently [95]. Even in the low-COR scenario, the CO-concentration in the reactor increases slightly at reactor entry, and CO-consumption towards $CO_2$-generation and subsequent hydrogenation towards MeOH only begins after a sufficient CO-partial pressure of approx. 3 bar is reached. This is in line with the fitting results omitting CO-hydrogenation for the optimized model, as all reactions pathways in the reactor are directly assigned to either WGS/RWGS or $CO_2$-hydrogenation reactions and CO-consumption and -production are not calculated through the CO-hydrogenation pathway to MeOH. 20% CZCZ show significantly increased reaction rates, as already discussed in Section 3.2. Consequently, initial $CO_2$-consumption is considerably higher, with species concentration for MeOH and $H_2O$ reaching an equilibrium earlier though, barely changing after approx 50% axial reactor length. CaO-promotion in 20% CZCZC changes the mathematical kinetics of the model the most. With overall smoother gradients across the reactor length. The subplots for 20% CZCZC suggest, that the reactions involved in $CO_2$- and CO conversion do not reach equilibrium in the herein used reactor setup, implying that changed reactor geometries in the test setup could have contributed to slightly increased $X_C$ for 20% CZCZC in this work.

Sensitivity of the models towards parameter changes was investigated in order to evaluate single- and multi-parameter impact on the model results. For each model, the sensitivity of output parameters, such as $X_{CO2}$, $STY_{MeOH}$, $STY_{H2O}$ and $S_{MeOH}$ were tested against perturbation of single parameter classes of 10%. Table 9 shows the model sensitivity towards single parameters that were chosen for their high impact on model results. For each individual kinetic model, the sensitivity towards changes of 10% in the parameter values for the pre-exponential factor of MeOH-formation from $CO_2$, activation energy for RWGS, pre-exponential, consolidated factor for the adsorption term of $CO_2$ and adsorption energy of $CO_2$-adsorption as well as the pre-exponential factor in the adsorption term for $H_2O$ are tested under high COR conditions for SN = 2.0. The models for 20% CZCZ and 20% CZCZC show high robustness towards parametric changes. This indicates low influence of the probed parameters towards the model

outcome and suggests parametric uncertainty to a degree. 20% CZ and 20% CZC have more sensitive models towards most of the tested factors. This implicates more certain model fit towards these parameters and underlines the fit quality of the models fitted to the test data of 20% CZ and 20% CZC. Overall, sensitivity is moderate, suggesting more in depth review of the modeled data could be the foundation of a parameter reduction in those parameters for which the optimized models exhibit low sensitivity [44].

## 4. Conclusion

In this work, we presented a detailed performance analysis, a substantial extension of physio-chemical characterization and a parameter fitting for an existing kinetic model for four previously prepared and reported infiltration composite catalysts for the effective conversion of CO and $CO_2$ to MeOH. We investigated the catalysts through the analysis of radial FIB-Lamellae of the spheres, Raman- and XPS-spectra of the catalyst surfaces as well as adsorption and desorption properties for $H_2$- and $CO_2$. Physical surface properties were tested in unreduced samples, constituting a limitation of this work, but still lending valuable insights into coating efficiency of $\gamma$-alumina spheres with catalytically highly active metal oxides and their resulting surface structures. Additionally, we tested the catalyst performances in mixed carbon-oxide environments, as are expectable in industrial regenerative MeOH-synthesis with $CO_2$ as main carbon source and process gas recycling. The $CeO_2$, $ZrO_2$ and CaO promoted catalysts show large interfacial areas between different metal-oxide agglomerates on the $\gamma$-$Al_2O_3$ carrier spheres. This is indicative of the formation of active centers for both the adsorption of CO as well as $CO_2$. Raman- and XPS-analysis confirm the correct loading and metal-oxide ratios on the catalyst surfaces. Additionally, XPS-analysis indicated heightened dispersion and more complex metal-metal-oxide interaction on the catalyst surface, which is in line with the presented TEM-imaging. The physical findings are supported by the test results from mixed carbon-oxide SynGas testing. Here all catalyst samples perform well, with the $CeO_2$ and $ZrO_2$ promoted 20% CZCZ catalyst performing the best concerning $STY_{MeOH}$, showing good MeOH-production rates throughout different tested SynGas COR, pressures and reactor temperatures. This finding is especially important, as all samples were only coated with 20%w active catalyst phase with catalyst densities considerably lower than for co-precipitated commercial catalyst samples. This suggests, that only part of the active phase in precipitated catalyst samples actually contributes to the heterogeneous catalytic reactions and lays an important foundation for future development of efficient catalyst formulations. Additionally, an existing kinetic model for modeling the MeOH synthesis is re-parametrized based upon the herein presented testing result and provided open source, delivering a good and efficient approach for future kinetic work in catalysis. Mathematically, MeOH formation from CO is omitted from the numerical model, which is in line with previous findings in $CO_2$-hydrogenation to MeOH. An effective kinetic parameter set was determined for every sample, enabling the calculation of complex tubular reactor models and future work in scale-up for catalytic applications. The models suggests the conversion of $CO_2$ to MeOH via the formate route, with the hydrogenation of adsorbed $HCOO^*$s or the hydrogenation of $H_2OO$ $*$-species being mathematically determined as rate determining in MeOH formation. Meanwhile, the models suggest that CO acts as $H_2O$ scavenger, with adsorbed $H_2O$ species necessary to activate CO on the catalyst surfaces in RWGS-reaction mechanisms. Overall, this work presents the basis for an extended understanding of how different popular MeOH-catalyst promoters interact in different formulas in carrier catalyst applications. The classic CuO/ZnO catalyst complex performs well in CO-dominated SynGas streams, $CeO_2$ and $ZrO_2$ are nonetheless able to improve conversion performance, especially in $CO_2$-rich synthesis gas applications.

## CRediT authorship contribution statement

**Carl Fritsch:** Writing – original draft, Visualization, Validation, Resources, Project administration, Investigation, Funding acquisition, Formal analysis, Conceptualization. **Andreas Serwe:** Investigation, Formal analysis. **Sven Jovanovic:** Writing – review & editing, Investigation. **Hariprasad Ranganathan:** Writing – review & editing, Investigation. **Marcus Hans:** Writing – review & editing, Investigation, Formal analysis. **Andreas Hutzler:** Writing – review & editing, Investigation, Formal analysis. **Jürgen Dornseiffer:** Writing – review & editing, Investigation, Conceptualization. **Nikolay Kornienko:** Writing – review & editing, Resources.

## Declaration of generative AI and AI-assisted technologies in the manuscript preparation process

During the preparation of this work the authors used Claude LLM Model 4.2 in order to source, correct and optimize the python code for parameter optimization and statistical analysis of the data gathered in the laboratory tests. After using this tool/service, the authors reviewed and edited the content as needed and take full responsibility for the content of the published article. The code is made available open source along side this publication and can be found here: https://github.com/Fircar/Kinetics-Optimization.

## Declaration of competing interest

The authors declare that they have no known competing financial interests or personal relationships that could have appeared to influence the work reported in this paper.

## Appendix A. Supplementary data

Supplementary material related to this article can be found online at https://doi.org/10.1016/j.apcata.2025.120675.

## Data availability

Data will be made available on request.

## References

[1] V. Dieterich, A. Buttler, A. Hanel, H. Spliethoff, S. Fendt, Power-to-liquid via synthesis of methanol, DME or fischer–tropsch-fuels: a review, Energy & Environ. Sci. 13 (10) (2020) 3207–3252.
[2] M. Ebrahimzadeh Sarvestani, O. Norouzi, F. Di Maria, A. Dutta, From catalyst development to reactor design: A comprehensive review of methanol synthesis techniques, Energy Convers. Manage. 302 (2024) 118070.
[3] T. Biswal, K.P. Shadangi, P.K. Sarangi, R.K. Srivastava, Conversion of carbon dioxide to methanol: A comprehensive review, Chemosphere 298 (2022) 134299.
[4] Y. Khojasteh-Salkuyeh, O. Ashrafi, E. Mostafavi, P. Navarri, CO2 utilization for methanol production; part I: Process design and life cycle GHG assessment of different pathways, J. CO2 Util. 50 (2021) 101608.
[5] X. Jiang, X. Nie, X. Guo, C. Song, J.G. Chen, Recent advances in carbon dioxide hydrogenation to methanol via heterogeneous catalysis, Chem. Rev. 120 (15) (2020) 7984–8034.
[6] N.J. Azhari, D. Erika, S. Mardiana, T. Ilmi, M.L. Gunawan, I. Makertihartha, G.T. Kadja, Methanol synthesis from CO2: A mechanistic overview, Results Eng. 16 (2022) 100711.
[7] A. Beck, M.A. Newton, L.G.A. van de Water, J.A. van Bokhoven, The enigma of methanol synthesis by Cu/ZnO/Al2O3-based catalysts, Chem. Rev. 124 (8) (2024) 4543–4678.
[8] A. Cao, Z. Wang, H. Li, A.O. Elnabawy, J.K. Nørskov, New insights on CO and CO2 hydrogenation for methanol synthesis: The key role of adsorbate-adsorbate interactions on Cu and the highly active MgO-Cu interface, J. Catalysis 400 (2021) 325–331.
[9] L.C. Grabow, M. Mavrikakis, Mechanism of methanol synthesis on cu through CO2 and CO hydrogenation, ACS Catal. 1 (4) (2011) 365–384.
[10] N.D. Nielsen, A.D. Jensen, J.M. Christensen, The roles of CO and CO2 in high pressure methanol synthesis over Cu-based catalysts, J. Catalysis 393 (2021) 324–334.

[11] C. Fritsch, J. Dornseiffer, J. Blankenstein, M. Noyong, C. Groteklaes, U. Simon, CO 2 –hydrogenation to methanol over CuO/ZnO based infiltration composite catalyst spheres, ChemCatChem 16 (21) (2024).
[12] J. Zhu, Y. Su, J. Chai, V. Muravev, N. Kosinov, E.J.M. Hensen, Mechanism and nature of active sites for methanol synthesis from CO/CO 2 on Cu/CeO 2, ACS Catal. 10 (19) (2020) 11532–11544.
[13] M. Ren, Y. Zhang, X. Wang, H. Qiu, Catalytic hydrogenation of CO2 to methanol: A review, Catalysts 12 (4) (2022) 403.
[14] F. Nestler, J. Full, J.-M. Jäckle, J. Linsenmeier, J. Roob, M.J. Hadrich, A. Schaadt, Experimental validation of methanol synthesis from steel mill gases using a miniplant setup, Chem. Ing. Tech. 94 (10) (2022) 1466–1475.
[15] D. Makhmutov, E. Fedorova, A. Zanina, C. Kubis, D. Zhao, D. Doronkin, N. Rockstroh, S. Bartling, U. Armbruster, S. Wohlrab, E.V. Kondratenko, Reaction pathways of methanol formation in CO 2 hydrogenation over pd-based catalysts, ACS Catal. 15 (3) (2025) 2328–2341.
[16] F. Bisotti, M. Fedeli, K. Prifti, A. Galeazzi, A. Dell'Angelo, F. Manenti, Impact of kinetic models on methanol synthesis reactor predictions: In silico assessment and comparison with industrial data, Ind. Eng. Chem. Res. 61 (5) (2022) 2206–2226.
[17] K. Li, J.G. Chen, CO 2 hydrogenation to methanol over ZrO 2 -containing catalysts: Insights into ZrO 2 induced synergy, ACS Catal. 9 (9) (2019) 7840–7861.
[18] M. Zabilskiy, K. Ma, A. Beck, J.A. van Bokhoven, Methanol synthesis over Cu/CeO 2 –ZrO 2 catalysts: the key role of multiple active components, Catal. Sci. Technol. 11 (1) (2021) 349–358.
[19] X. Zhang, X. Yu, R.G. Mendes, P. Matvija, A.E. Melcherts, C. Sun, X. Ye, B.M. Weckhuysen, M. Monai, Highly dispersed ZnO sites in a ZnO/ZrO2 catalyst promote the CO2-to-methanol reaction, 2024.
[20] R. Singh, K. Kundu, K.K. Pant, CO2 hydrogenation to methanol over Cu-ZnO-CeO2 catalyst: Reaction structure–activity relationship, optimizing Ce and Zn ratio, and kinetic study, Chem. Eng. J. 479 (2024) 147783.
[21] R. Ye, L. Ma, J. Mao, X. Wang, X. Hong, A. Gallo, Y. Ma, W. Luo, B. Wang, R. Zhang, M.S. Duyar, Z. Jiang, J. Liu, A Ce-CuZn catalyst with abundant Cu/Zn-OV-ce active sites for CO2 hydrogenation to methanol, Nat. Commun. 15 (1) (2024) 2159.
[22] J. Xiao, D. Mao, X. Guo, J. Yu, Effect of TiO2, ZrO2, and TiO2–ZrO2 on the performance of CuO–ZnO catalyst for CO2 hydrogenation to methanol, Appl. Surf. Sci. 338 (2015) 146–153.
[23] L.G. van de Water, S.K. Wilkinson, R.A. Smith, M.J. Watson, Understanding methanol synthesis from CO/H2 feeds over Cu/CeO2 catalysts, J. Catalysis 364 (2018) 57–68.
[24] W. Wang, X. Zhang, M. Guo, J. Li, C. Peng, An investigation of the CH3OH and CO selectivity of CO2 hydrogenation over Cu–Ce–Zr catalysts, Front. Chem. Sci. Eng. 16 (6) (2022) 950–962.
[25] W.L. Ng, P. Sripada, S. Biswas, S. Bhattacharya, Experimental work and kinetic modelling of CO2 hydrogenation to methanol on CeO2 supported In2O3 catalyst, Appl. Catal. A: Gen. 646 (2022) 118885.
[26] C. Wu, L. Lin, J. Liu, J. Zhang, F. Zhang, T. Zhou, N. Rui, S. Yao, Y. Deng, F. Yang, W. Xu, J. Luo, Y. Zhao, B. Yan, X.-D. Wen, J.A. Rodriguez, D. Ma, Inverse ZrO2/Cu as a highly efficient methanol synthesis catalyst from CO2 hydrogenation, Nat. Commun. 11 (1) (2020) 5767.
[27] T. Witoon, T. Numpilai, T. Phongamwong, W. Donphai, C. Boonyuen, C. Warakulwit, M. Chareonpanich, J. Limtrakul, Enhanced activity, selectivity and stability of a CuO-ZnO-ZrO2 catalyst by adding graphene oxide for CO2 hydrogenation to methanol, Chem. Eng. J. 334 (2018) 1781–1791.
[28] X. Dong, F. Li, N. Zhao, F. Xiao, J. Wang, Y. Tan, CO2 hydrogenation to methanol over Cu/ZnO/ZrO2 catalysts prepared by precipitation-reduction method, Appl. Catal. B: Environ. 191 (2016) 8–17.
[29] V.D. Dasireddy, N.S. Štefančič, M. Huš, B. Likozar, Effect of alkaline earth metal oxide (MO) Cu/MO/Al2O3 catalysts on methanol synthesis activity and selectivity via CO2 reduction, Fuel 233 (2018) 103–112.
[30] C. Zhong, X. Guo, D. Mao, S. Wang, G. Wu, G. Lu, Effects of alkaline-earth oxides on the performance of a CuO–ZrO 2 catalyst for methanol synthesis via CO 2 hydrogenation, RSC Adv. 5 (65) (2015) 52958–52965.
[31] S. Poto, D. van Vico Berkel, F. Gallucci, M. Fernanda Neira d'Angelo, Kinetic modelling of the methanol synthesis from CO2 and H2 over a CuO/CeO2/ZrO2 catalyst: The role of CO2 and CO hydrogenation, Chem. Eng. J. 435 (2022) 134946.
[32] F. Salomone, E. Sartoretti, S. Ballauri, M. Castellino, C. Novara, F. Giorgis, R. Pirone, S. Bensaid, CO2 hydrogenation to methanol over Zr- and Ce-doped indium oxide, Catal. Today 423 (2023) 114023.
[33] H. Ren, C.-H. Xu, H.-Y. Zhao, Y.-X. Wang, J. Liu, J.-Y. Liu, Methanol synthesis from CO2 hydrogenation over Cug-Al2O3 catalysts modified by ZnO, ZrO2 and MgO, J. Ind. Eng. Chem. 28 (2015) 261–267.
[34] K. Xiao, Q. Wang, X. Qi, L. Zhong, For better industrial Cu/ZnO/Al2O3 methanol synthesis catalyst: A compositional study, Catal. Lett. 147 (6) (2017) 1581–1591.
[35] C.A. Schneider, W.S. Rasband, K.W. Eliceiri, NIH image to ImageJ: 25 years of image analysis, Nature Methods 9 (7) (2012) 671–675.
[36] M.B. Fichtl, O. Hinrichsen, On the temperature programmed desorption of hydrogen from polycrystalline copper, Catal. Lett. 144 (12) (2014) 2114–2120.
[37] M. Muhler, L.P. Nielsen, E. Trnqvist, B.S. Clausen, H. Topse, Temperature-programmed desorption of H2 as a tool to determine metal surface areas of Cu catalysts, Catal. Lett. 14 (3–4) (1992) 241–249.
[38] M.C. Amorim de Carvalho, F.B. Passos, M. Schmal, Quantification of metallic area of high dispersed copper on ZSM-5 catalyst by TPD of H2, Catal. Commun. 3 (11) (2002) 503–509.
[39] H. Zhou, H. Jin, Y. Li, Y. Li, S. Huang, W. Lin, W. Chen, Y. Zhang, Mechanism of methanol synthesis from CO2 hydrogenation over Cu/g-Al2O3 interface: Influences of surface hydroxylation, Catalysts 13 (9) (2023) 1244.
[40] M. Bowker, Methanol synthesis from CO2 hydrogenation, ChemCatChem 11 (17) (2019) 4238–4246.
[41] J.-F. Portha, K. Parkhomenko, K. Kobl, A.-C. Roger, S. Arab, J.-M. Commenge, L. Falk, Kinetics of methanol synthesis from carbon dioxide hydrogenation over copper–zinc oxide catalysts, Ind. Eng. Chem. Res. 56 (45) (2017) 13133–13145.
[42] F. Nestler, A.R. Schütze, M. Ouda, M.J. Hadrich, A. Schaadt, S. Bajohr, T. Kolb, Kinetic modelling of methanol synthesis over commercial catalysts: A critical assessment, Chem. Eng. J. 394 (2020) 124881.
[43] Ł. Hamryszak, M. Madej-Lachowska, M. Grzesik, M. Śliwa, Cu/Zn/Zr/Ga catalyst for utilisation of carbon dioxide to methanol—Kinetic equations, Catalysts 12 (7) (2022) 757.
[44] A. Kouzehli, M. Kazemeini, A. Ashrafi Moghaddam, A robust kinetic modeling of CO2 hydrogenation to methanol over an industrial copper–zinc oxide catalyst based on a single-active site mechanism, Int. J. Hydrog. Energy 60 (2024) 756–768.
[45] H.-W. Lim, M.-J. Park, S.-H. Kang, H.-J. Chae, J.W. Bae, K.-W. Jun, Modeling of the kinetics for methanol synthesis using Cu/ZnO/Al 2 O 3 /ZrO 2 catalyst: Influence of carbon dioxide during hydrogenation, Ind. Eng. Chem. Res. 48 (23) (2009) 10448–10455.
[46] N. Park, M.-J. Park, Y.-J. Lee, K.-S. Ha, K.-W. Jun, Kinetic modeling of methanol synthesis over commercial catalysts based on three-site adsorption, Fuel Process. Technol. 125 (2014) 139–147.
[47] G.H. Graaf, E.J. Stamhuis, A. Beenackers, Kinetics of low-pressure methanol synthesis, Chem. Eng. Sci. 43 (12) (1988) 3185–3195.
[48] S. Ghosh, J. Sebastian, L. Olsson, D. Creaser, Experimental and kinetic modeling studies of methanol synthesis from CO2 hydrogenation using In2O3 catalyst, Chem. Eng. J. 416 (2021) 129120.
[49] L. He, Y. Fan, L. Luo, J. Bellettre, J. Yue, Preparation of Pt/g-Al2O3 catalyst coating in microreactors for catalytic methane combustion, Chem. Eng. J. 380 (2020) 122424.
[50] D. Laudenschleger, H. Ruland, M. Muhler, Identifying the nature of the active sites in methanol synthesis over Cu/ZnO/Al2O3 catalysts, Nat. Commun. 11 (1) (2020) 3898.
[51] K. Lee, H. Yan, Q. Sun, Z. Zhang, N. Yan, Mechanism-guided catalyst design for CO2 hydrogenation to formate and methanol, Accounts Mater. Res. 4 (9) (2023) 746–757.
[52] F. Bisotti, M. Fedeli, K. Prifti, A. Galeazzi, A. Dell'Angelo, M. Barbieri, C. Pirola, G. Bozzano, F. Manenti, Century of technology trends in methanol synthesis: Any need for kinetics refitting? Ind. Eng. Chem. Res. 60 (44) (2021) 16032–16053.
[53] G.H. Graaf, J.G.M. Winkelman, Chemical equilibria in methanol synthesis including the water–gas shift reaction: A critical reassessment, Ind. Eng. Chem. Res. 55 (20) (2016) 5854–5864.
[54] C. Fritsch, Open source Python script for optimization of reaction kinetics, 2025.
[55] Z. Till, T. Varga, J. Sója, N. Miskolczi, T. Chován, Reduction of lumped reaction networks based on global sensitivity analysis, Chem. Eng. J. 375 (2019) 121920.
[56] I. Sobol', Global sensitivity indices for nonlinear mathematical models and their Monte Carlo estimates, Math. Comput. Simulation 55 (1–3) (2001) 271–280.
[57] S. Lin, M. Xie, J. Wang, W. Liang, C.K. Law, W. Zhou, B. Yang, Chemical kinetic model reduction through species-targeted global sensitivity analysis (STGSA), Combust. Flame 224 (2021) 73–82.
[58] B.C. Dharmalingam, A. Koushik V., M. Mureddu, L. Atzori, S. Lai, A. Pettinau, N.S. Kaisare, P. Aghalayam, J.J. Varghese, Unravelling the role of metal-metal oxide interfaces of Cu/ZnO/ZrO2/Al2O3 catalyst for methanol synthesis from CO2: Insights from experiments and DFT-based microkinetic modeling, Appl. Catal. B: Environ. 332 (2023) 122743.
[59] R.M. Palomino, P.J. Ramírez, Z. Liu, R. Hamlyn, I. Waluyo, M. Mahapatra, I. Orozco, A. Hunt, J.P. Simonovis, S.D. Senanayake, J.A. Rodriguez, Hydrogenation of CO2 on ZnO/Cu(100) and ZnO/cu(111) catalysts: Role of copper structure and metal-oxide interface in methanol synthesis, J. Phys. Chem. B 122 (2) (2018) 794–800.
[60] H. Zada, J. Yu, J. Sun, Active sites for CO2 hydrogenation to methanol: Mechanistic insights and reaction control, ChemSusChem 18 (4) (2025) e202401846.
[61] J. Xiao, D. Mao, G. Wang, X. Guo, J. Yu, CO2 hydrogenation to methanol over CuO ZnO TiO2ZrO2 catalyst prepared by a facile solid-state route: The significant influence of assistant complexing agents, Int. J. Hydrog. Energy 44 (29) (2019) 14831–14841.
[62] T. Armbruster, R. Danisi (Eds.), The power of databases: the RRUFF project, Highlights in Mineralogical Crystallography, W. De Gruyter, Berlin, 2015, URL https://rruff.info/about/downloads/HMC1-30.pdf.

[63] M. Varga, Á. Molnár, G. Mulas, M. Mohai, I. Bertóti, G. Cocco, Cu–MgO samples prepared by mechanochemistry for catalytic application, J. Catalysis 206 (1) (2002) 71–81.
[64] M. Nie, A. Cui, M. Wu, T. Guo, Q. Guo, CuO/LaCeOx catalysts with enhanced metal–support interactions for CO2 methanolization, J. CO2 Util. 75 (2023) 102579.
[65] H.Y. Chen, L. Chen, J. Lin, K.L. Tan, J. Li, Copper sites in copper-exchanged ZSM-5 for CO activation and methanol synthesis: XPS and FTIR studies, Inorg. Chem. 36 (7) (1997) 1417–1423.
[66] A.S. Haja Hameed, C. Karthikeyan, S. Sasikumar, V. Senthil Kumar, S. Kumaresan, G. Ravi, Impact of alkaline metal ions Mg2+, Ca2+, Sr2+ and Ba2+ on the structural, optical, thermal and antibacterial properties of ZnO nanoparticles prepared by the co-precipitation method, J. Mater. Chem. B 1 (43) (2013) 5950–5962.
[67] S. Kuld, M. Thorhauge, H. Falsig, C.F. Elkjær, S. Helveg, I. Chorkendorff, J. Sehested, Quantifying the promotion of Cu catalysts by ZnO for methanol synthesis, Sci. (New York, N.Y.) 352 (6288) (2016) 969–974.
[68] T. Lunkenbein, F. Girgsdies, T. Kandemir, N. Thomas, M. Behrens, R. Schlögl, E. Frei, Bridging the time gap: A copper/zinc oxide/aluminum oxide catalyst for methanol synthesis studied under industrially relevant conditions and time scales, Angew. Chem. (Int. Ed. English) 55 (41) (2016) 12708–12712.
[69] A. Ruiz Puigdollers, P. Schlexer, S. Tosoni, G. Pacchioni, Increasing oxide reducibility: The role of metal/oxide interfaces in the formation of oxygen vacancies, ACS Catal. 7 (10) (2017) 6493–6513.
[70] J. Li, M. Nolan, C. Detavernier, A step towards correct interpretation of XPS results in metal oxides: a case study aided by first-principles method in ZnO, 2023.
[71] C. Mendoza-Merlano, J. Tapia-Pérez, E. Serna-Galvis, D. Hoyos-Ayala, J. Arboleda-Echavarría, A. Echavarría-Isaza, Improved conversion, selectivity, and stability during CO2 methanation by the incorporation of Ce in Ni, Co, and fe-hydrotalcite-derived catalysts, Int. J. Hydrog. Energy 60 (2024) 985–995.
[72] D. Chen, D. Mao, J. Xiao, X. Guo, J. Yu, CO 2 hydrogenation to methanol over CuO–ZnO–TiO2–ZrO2: a comparison of catalysts prepared by sol–gel, solid-state reaction and solution-combustion, J. Sol-Gel Sci. Technol. 86 (3) (2018) 719–730.
[73] Y. Wang, H. Ban, Y. Wang, R. Yao, S. Zhao, J. Hu, C. Li, Unraveling the role of basic sites in the hydrogenation of CO2 to formic acid over Ni-based catalysts, J. Catalysis 430 (2024) 115357.
[74] P. Gao, F. Li, N. Zhao, F. Xiao, W. Wei, L. Zhong, Y. Sun, Influence of modifier (Mn, La, Ce, Zr and Y) on the performance of Cu/Zn/Al catalysts via hydrotalcite-like precursors for CO2 hydrogenation to methanol, Appl. Catal. A: Gen. 468 (2013) 442–452.
[75] J.T. Miller, B.L. Meyers, F.S. Modica, G.S. Lane, M. Vaarkamp, D.C. Koningsberger, Hydrogen temperature-programmed desorption (H2 TPD) of supported platinum catalysts, J. Catalysis 143 (2) (1993) 395–408.
[76] Y. Chen, S. Li, S. Lv, Y. Huang, A novel synthetic route for MOF-derived CuO-CeO2 catalyst with remarkable methanol steam reforming performance, Catal. Commun. 149 (2021) 106215.
[77] T.P. Araújo, A.H. Hergesell, D. Faust-Akl, S. Büchele, J.A. Stewart, C. Mondelli, J. Pérez-Ramírez, Methanol synthesis by hydrogenation of hybrid CO2 -CO feeds, ChemSusChem 14 (14) (2021) 2914–2923.
[78] J. Han, L. Wang, J. Yu, M. Fan, D. Mao, CO2 hydrogenation to methanol over Cu-CeO2-ZrO2 catalysts: The significant effect of metal-support interaction, Fuel 381 (2025) 133262.
[79] Y.-F. Shi, P.-L. Kang, C. Shang, Z.-P. Liu, Methanol synthesis from CO2/CO mixture on Cu-Zn catalysts from microkinetics-guided machine learning pathway search, J. Am. Chem. Soc. 144 (29) (2022) 13401–13414.
[80] S. Asthana, K. Tripathi, K.K. Pant, Impact of la engineered stable phase mixed precursors on physico-chemical features of Cu- based catalysts for conversion of CO2 rich syngas to methanol, Catal. Today 404 (2022) 154–168.
[81] F. Studt, M. Behrens, E.L. Kunkes, N. Thomas, S. Zander, A. Tarasov, J. Schumann, E. Frei, J.B. Varley, F. Abild-Pedersen, J.K. Nørskov, R. Schlögl, The mechanism of CO and CO 2 hydrogenation to methanol over Cu–based catalysts, ChemCatChem 7 (7) (2015) 1105–1111.
[82] Q. Maqbool, K. Dobrezberger, J. Stropp, M. Huber, K.-L. Kontrus, A. Aspalter, J. Neuhauser, T. Schachinger, S. Löffler, G. Rupprechter, Bimetallic CuPd nanoparticles supported on ZnO or graphene for CO2 and CO conversion to methane and methanol, RSC Sustain. 2 (11) (2024) 3276–3288.
[83] I.U. Din, M.A. Alotaibi, A.I. Alharthi, Green synthesis of methanol over zeolite based cu nano-catalysts, effect of Mg promoter, Sustain. Chem. Pharm. 16 (2020) 100264.
[84] W.J. Lee, A. Bordoloi, J. Patel, T. Bhatelia, The effect of metal additives in Cu/Zn/Al2O3 as a catalyst for low-pressure methanol synthesis in an oil-cooled annulus reactor, Catal. Today 343 (2020) 183–190.
[85] V. Pandey, P.P. Singh, K.K. Pant, S. Upadhyayula, S. Sengupta, Promotional role of methanol and CO2 in carbon dioxide-rich syngas hydrogenation over slurry reactor utilizing combustion induced Cu-based catalysts, Mater. Today Sustain. 29 (2025) 101082.
[86] J. Zuo, W. Na, P. Zhang, X. Yang, J. Wen, M. Zheng, H. Wang, Enhanced activity of CexZr1-xO2 solid solutions supported cu-based catalysts for hydrogenation of CO2 to methanol, Mol. Catal. 526 (2022) 112357.
[87] H. Ban, C. Li, K. Asami, K. Fujimoto, Influence of rare-earth elements (La, Ce, Nd and Pr) on the performance of Cu/Zn/Zr catalyst for CH3OH synthesis from CO2, Catal. Commun. 54 (2014) 50–54.
[88] G. Wang, D. Mao, X. Guo, J. Yu, Methanol synthesis from CO2 hydrogenation over CuO-ZnO-ZrO2-MxOy catalysts (M=Cr, Mo and W), Int. J. Hydrog. Energy 44 (8) (2019) 4197–4207.
[89] C. Huang, D. Mao, X. Guo, J. Yu, Microwave–assisted hydrothermal synthesis of CuO–ZnO–ZrO 2 as catalyst for direct synthesis of methanol by carbon dioxide hydrogenation, Energy Technol. 5 (11) (2017) 2100–2107.
[90] T. Vergara, D. Gómez, B. Lacerda de Oliveira Campos, K. Herrera Delgado, P. Concepción, R. Jiménez, A. Karelovic, Combined role of ce promotion and TiO2 support improves CO2 hydrogenation to methanol on Cu catalysts: Interplay between structure and kinetics, J. Catalysis 426 (2023) 200–213.
[91] W. Ding, J. Li, F. Li, Q. Tang, W. Fang, Thorium-promoted Cu/Zn/Al syngas catalyst for methanol synthesis with enhanced activity and stability, Fuel 367 (2024) 131470.
[92] Q. Zhang, X. Li, K. Fujimoto, Pd-promoted Cr/ZnO catalyst for synthesis of methanol from syngas, Appl. Catal. A: Gen. 309 (1) (2006) 28–32.
[93] M.M.-J. Li, Z. Zeng, F. Liao, X. Hong, S.C.E. Tsang, Enhanced CO2 hydrogenation to methanol over CuZn nanoalloy in Ga modified Cu/ZnO catalysts, J. Catalysis 343 (2016) 157–167.
[94] Y. Slotboom, M.J. Bos, J. Pieper, V. Vrieswijk, B. Likozar, S. Kersten, D. Brilman, Critical assessment of steady-state kinetic models for the synthesis of methanol over an industrial Cu/ZnO/Al2O3 catalyst, Chem. Eng. J. 389 (2020) 124181.
[95] G. Leonzio, Mathematical modeling of a methanol reactor by using different kinetic models, J. Ind. Eng. Chem. 85 (2020) 130–140.